

**Development of Numerical Simulation Methods for Analysis of  
Laser Guided Arc Discharge**

**William Page  
Brian Fisk  
William Zimmerman**

**29 February 2008**

**Final Report**

Approved for public release; distribution is unlimited.



**AIR FORCE RESEARCH LABORATORY  
Directed Energy Directorate  
3550 Aberdeen Ave SE  
AIR FORCE MATERIEL COMMAND  
KIRTLAND AIR FORCE BASE, NM 87117-5776**

## **DTIC COPY**

### **NOTICE AND SIGNATURE PAGE**

Using Government drawings, specifications, or other data included in this document for any purpose other than Government procurement does not in any way obligate the U.S. Government. The fact that the Government formulated or supplied the drawings, specifications, or other data does not license the holder or any other person or corporation; or convey any rights or permission to manufacture, use, or sell any patented invention that may relate to them.

This report was cleared for public release by the Office of Public Affairs, 377<sup>th</sup> ABW, for the Air Force Research Laboratory, Phillips Research Site, and is available to the general public, including foreign nationals. Copies may be obtained from the Defense Technical Information Center (DTIC) (<http://www.dtic.mil>).

AFRL-RD-PS-TR-2008-1041 HAS BEEN REVIEWED AND IS APPROVED FOR PUBLICATION IN ACCORDANCE WITH ASSIGNED DISTRIBUTION STATEMENT.

//signed//

---

DR. WILLIAM PAGE, DR-III  
Program Manager

//signed//

---

DR. WALLACE T. CLARK III, DR-IV  
Chief, Laser Division

This report is published in the interest of scientific and technical information exchange, and its publication does not constitute the Government's approval or disapproval of its ideas or findings.

REPORT DOCUMENTATION PAGE				Form Approved OMB No. 0704-0188	
Public reporting burden for this collection of information is estimated to average 1 hour per response, including the time for reviewing instructions, searching existing data sources, gathering and maintaining the data needed, and completing and reviewing this collection of information. Send comments regarding this burden estimate or any other aspect of this collection of information, including suggestions for reducing this burden to Department of Defense, Washington Headquarters Services, Directorate for Information Operations and Reports (0704-0188), 1215 Jefferson Davis Highway, Suite 1204, Arlington, VA 22202-4302. Respondents should be aware that notwithstanding any other provision of law, no person shall be subject to any penalty for failing to comply with a collection of information if it does not display a currently valid OMB control number. <b>PLEASE DO NOT RETURN YOUR FORM TO THE ABOVE ADDRESS.</b>					
1. REPORT DATE (DD-MM-YYYY) 29-February-2008		2. REPORT TYPE Final Report		3. DATES COVERED (From - To) 3-February-2006 – 28-February-2008	
4. TITLE AND SUBTITLE  Development of Numerical Simulation Methods for Analysis of Laser Guided Arc Discharge				5a. CONTRACT NUMBER In-House (DF297612)	
				5b. GRANT NUMBER	
				5c. PROGRAM ELEMENT NUMBER 63605F	
6. AUTHOR(S)  William Page, Brian Fisk*, William Zimmerman*				5d. PROJECT NUMBER 3151	
				5e. TASK NUMBER LS	
				5f. WORK UNIT NUMBER 02	
7. PERFORMING ORGANIZATION NAME(S) AND ADDRESS(ES)  AFRL/RDLS 3550 Aberdeen Ave SE Kirtland AFB NM 87117-5776				8. PERFORMING ORGANIZATION REPORT NUMBER	
9. SPONSORING / MONITORING AGENCY NAME(S) AND ADDRESS(ES)  Air Force Research Laboratory 3550 Aberdeen Ave SE Kirtland AFB NM 87117-5776				10. SPONSOR/MONITOR'S ACRONYM(S)	
				11. SPONSOR/MONITOR'S REPORT NUMBER(S) AFRL-RD-PS-TR-2008-1041	
12. DISTRIBUTION / AVAILABILITY STATEMENT Approved for public release; distribution is unlimited.					
13. SUPPLEMENTARY NOTES *ITT-AES, 5901 Indian School NE , Albuquerque NM 87110					
14. ABSTRACT: Modeling of the use of USP laser pre-ionization as a guide path for a high voltage discharge in air was addressed. The physical processes involved are complex and span many orders of magnitude in the temporal and spatial resolution that must be considered. A two dimensional simulation model was produced that treats the problem in different time regimes with suitable approximations. The theoretical models and numerical models developed are described along with some test calculations. The simulations were done on a single CPU PC workstation. Procedures were outlined for porting the simulation to a multi-node high performance computer.					
15. SUBJECT TERMS Directed Energy (DE), Infrared Countermeasure (IRCM), Focal Plane Array (FPA) damage					
16. SECURITY CLASSIFICATION OF:			17. LIMITATION OF ABSTRACT	18. NUMBER OF PAGES	19a. NAME OF RESPONSIBLE PERSON
a. REPORT Unclassified	b. ABSTRACT Unclassified	c. THIS PAGE Unclassified			William Page
			SAR	46	19b. TELEPHONE NUMBER (include area code)
Standard Form 298 (Rev. 8-98) Prescribed by ANSI Std. Z39.18					



# TABLE OF CONTENTS

<b>Section</b>	<b>Page</b>
1.0 Introduction	1
2.0 Theoretical Formulation	9
3.0 Numerical Formulation	21
4.0 Test Simulations	33
5.0 Conclusions	36
6.0 References	37

## LIST OF FIGURES

Figure		Page
Figure 1.	Schematic view of the electrical breakdown problem	1
Figure 2.	Simulation geometry used for numerical simulation of the electrical breakdown and ionization guided Arc.	4
Figure 3.	Timing comparison of FFT-based and SOR Methods.	6
Figure 4.	Scheme for implementing snapshot calculation for extended ranges	8
Figure 5.	Numerical grid for the two dimensional problem	21
Figure 6.	Placement of a potential surface in the finite difference grid	22
Figure 7.	Representation of the finite difference conductivity/resistivity mesh used to solve for the late time discharge	31
Figure 8.	First Run Charge Density	33
Figure 9.	First Run Scalar Potential	33
Figure 10.	Analytic Scalar Potential for a Uniformly Charge Sphere	35
Figure 11.	Difference between Analytic and Fast Poisson Solutions	35
Figure 12.	Difference between Analytic and Fast Poisson Solutions	35
Figure 13.	Scalar Potential for Second Test Case	35

## 1.0 Introduction

### Acknowledgement

This effort was supported in part by the US Air Force Office of Scientific Research, Mathematical Sciences Division

### Motivation

There has been a considerable amount of work done on understanding, modeling and computing the observed self focusing and ionization of ultra short laser pulses (USP) when they propagate in air and other materials. There is a need for study of the potential applications of these effects. One application that has been suggested is the use of a USP ionization channel to guide and extend the length of high voltage electrical arcs. Although there are questions about the feasible utility of this idea (Ref 1), we need to develop new physics models and analysis techniques for assessing this utilization.

### Background Discussion

Modeling of USP laser pulse propagation with self focusing and ionization has been done previously Braun (Ref 2), Mlejnick (Ref 3), and Sprangle (Ref 4). A study was done at AFRL/DE in order to understand the reported associated EMP radiation. Analytical estimates were discussed and a numerical atmospheric propagation code was developed, based on standard pulse envelope techniques outlined in (Ref 4). The modeling effort also included development of a full Maxwell's Equation model for propagation and material interaction. This modeling and computational simulation development has been published in (Ref 1).

The possibility of electrical energy discharge guided by an USP produced ionization channel in air has been raised. As an example the positive terminal of a high voltage source may be connected to a conductor in close proximity to the filament produced in air by an ultra short laser and the return electrode may consist of the target, and the material that the target is standing on. Although the use of Ultra-Violet (UV) lasers to trigger electrical breakdown is well-known, ultra short laser produced filaments would appear to offer an advantage in precise control of the location and direction of the electrical breakdown. Experiments performed to date have shown some promise but a satisfactory modeling capability is necessary to guide experiments and to assess the viability of potential practical uses.

The scope of this project included the formulation of an overall simulation methodology and the development, testing and integration of the requisite sub models. It did not include porting to, and parallel operation on, a High Performance Computer (HPC) platform. This will be required to determine the ultimate length of streamer propagation and the energy delivery to an anode for cases of practical application.

### Problem Overview

In the current effort an electrical discharge model was developed to describe the USP induced breakdown of a spark gap at ambient conditions. The problem geometry is shown in Figure 1.

The USP induced ionization is schematically represented by the arrows between the two disk electrodes.

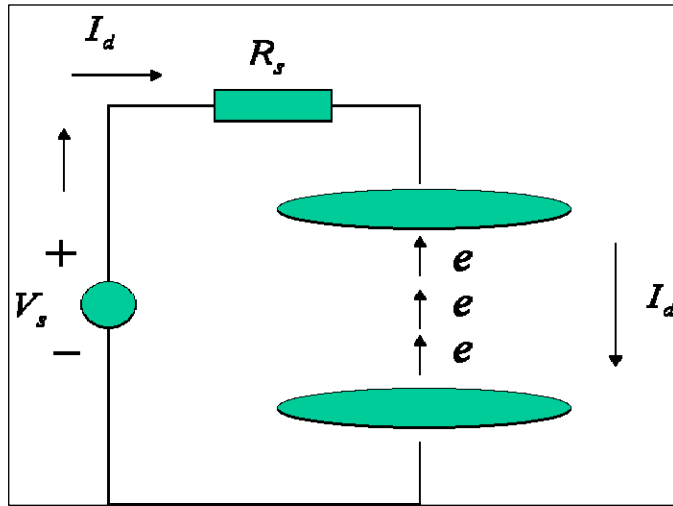


Figure 1. Schematic view of the electrical breakdown problem.

The problem of predicting the time behavior of an electrical discharge has been widely studied by many investigators and is still not fully understood. Examples of electrical discharges range from the local corona discharge induced on high voltage transmission lines, to the long spark spanning a gap with dimensions of centimeters to tens of meters, to the phenomena of natural lightning. The problem is recognized to be difficult due to the large range of dimensions and time scales involved, as well as an incomplete understanding of all the relevant physics.

The physics of electrical breakdown in a one-dimensional planar geometry was studied by Kline [Ref. 5] using Monte-Carlo techniques. The velocities of anode and cathode directed streamers in nitrogen at relatively low pressures were compared to experiment. Of particular interest was the use of the empirical results of Penny [Ref. 6] to determine the photo ionization rates in nitrogen. Monte Carlo methods have also been demonstrated by Kunhardt [Ref. 7] and others. The Monte Carlo approach has the obvious advantage of being able to represent the six dimensional distribution function of the electrons and ions. However the method is computationally intense as the random velocity of the electron distribution has to be properly advanced over a spatial grid with relatively small length scales. As a result much effort has been put into developing models that effectively integrate over the distribution function and advance the electron and ion drift velocities. These approaches either use the electron and ion mobilities by Yoshida [Ref. 8], Wu [Ref. 9], Wang [Ref. 10], Vitello [Ref. 11], Kulikovskiy [Ref. 12], or solve the electron swarm equations by Guo [Ref. 13].

In the calculations described here the ionization path produced by the self focusing propagation of ultra short laser pulses was included as a fixed (time independent pre-ionization). Time dependant laser ionization during the formation of the discharge channel can easily be added. The levels of the USP laser ionization used were taken from previous studies of self focusing propagation by Zimmerman, et al [Ref. 1].



The use of electron and ion mobilities to relate the electron and ion velocities directly to the local electric field strength is commonly referred to as the equilibrium approach as it assumes the electron and ion have come into equilibrium between the effective collision frequencies and the acceleration of the electric field. The use of a full set of fluid equations to model the electrons and ions is referred to as the non-equilibrium approach and is more demanding on computer resources and may be more susceptible to instabilities when the electron plasma frequency approaches the inverse of the time step. Although neither approach has the fidelity of a full Monte Carlo simulation of the electron and ion distribution functions both the equilibrium and non-equilibrium approaches are felt to be adequate for electrical breakdown problems due to the simple fact that the electrons and ions travel “one way” between the cathode and anode (or visa-versa).

The majority of papers referenced above consider breakdown in nitrogen and do not consider late time heating and arcing effects. Arcing by itself has been studied by Plooster [Ref. 14] and Ganesh [Ref. 15] but the models used are typically one dimensional radial models and consider thermal and hydrodynamic effects at relatively late times as compared to the streamer breakdown problem. There has been more recent interest in modeling electrical breakdown in air and incorporating a more complete description of the complex air chemistry; see Kossyi [Ref.16], Naidis [Ref. 17], Aleksandrov [ref. 18]. Many of the simulations are 1½ D where the streamer radius is fixed. The behavior of a long leader in air has been studied using 1D radial models Aleksandrov, [Ref. 19] and [Ref. 207] and a 1½ D model, Aleksandrov [Ref. 21]. The 1½ D or quasi 2D simulations are often preferred as the spatial grid requirements and the need to solve the stiff system of complex air chemistry makes the problem computationally challenging. A contemporary review of the subjects of spark discharge and air chemistry can be found in Bazelyan and Raizer [Ref. 22] and Capitelli [Ref.23].

In this report we will be interested in the problem of the initiation of an electrical discharge by means of a laser induced ionized path between two oppositely charged electrodes in air at atmospheric pressure. In addition we are interested in both the early time streamer dynamics as well as the development of a hot electrically conductive leader channel that allows the electrical breakdown to travel over large distances. The problem, as illustrated in Figure 1, consists of a spark gap constructed of two cylindrical electrodes separated by a distance  $d$ . The spark gap is driven by a voltage source  $V_s$  with a series impedance  $R_s$  resulting in voltages  $V_u, V_l$  on the upper and lower plates. A laser is used to create a channel of ionization along the axis. The problem is to predict the time history of the electrical discharge including the discharge current  $I_g$  and the voltage drop  $V_g = V_u - V_l$  across the electrodes.

### Modeling Approach

The modeling approach described here divides the electrical breakdown problem into a sequential set of calculations based on the time scale and the physical mechanisms of the problem. Specifically we will divide the problem into an early time and a late time regime.

**Early Time Phase:** The initial electrical breakdown problem consists of the electron avalanche resulting in space charge waves. Depending on the details of the electrodes and the use of a laser

for pre-ionization it is necessary to consider electron transport, ion transport and diffusion. In this report the early time electron motion will be modeled with a fluid approach. It will be necessary to consider various source terms including avalanche, electron attachment and electron-ion recombination. During the early time phase of the electrical discharge the electron temperature will not be in equilibrium with the ion and neutral temperatures.

**Late Time Phase:** During the later part of the breakdown process the neutral gas is expected to become hot enough so that thermal agitation accounts for most of the free charge. In this case we will assume thermal equilibrium between the electrons, ions and neutral gas molecules and atoms and use an electrical conductivity to model the final breakdown process.

A two dimensional numerical model in cylindrical coordinates will be developed to model the electrical discharge problem. In addition a one-dimensional model will be developed. The one-dimensional model is relatively easy to understand and so is useful for developing and testing numerical methods and physical assumptions.

### Simulating a Laser Induced Electrical Discharge

The problem of interest is determining whether a laser trigger electrical discharge can propagate over a distance of several meters. As will be shown, the early time breakdown problem will require ~5-10 micron resolution over the dimensions of the head of the discharge. This dimension is on the order of centimeters. As a result it is not possible, nor necessary to actually simulate the entire discharge process. Instead the approach taken in simulating the nuclear induced lightning problem by Gardner [Ref.24] will be followed. To recall the nuclear lightning discharge involves the propagation of a streamer in the electrically conductive atmosphere induced by the prompted and delayed gamma radiation from a nuclear detonation. The approach used was to calculate the local discharge physics in a region of about 10 cm at the tip of a conductive streamer. If the numerical model showed that the discharge would propagate, rather than die out, then the simulation was successful. If necessary the simulation may be repeated for various streamer lengths.

### Model Geometries

A two dimensional simulation model was developed to model the propagation of a laser guided arc over short, centimeter scale, ranges. A secondary one dimensional model was also used to facilitate development and implementation of various physics sub models required for the complete simulation. The range limitation results from run time feasibility on single PC workstation computer. This range can be extended to the 10's of cm region by porting the model to a HPC. This procedure has been investigated and outlined but could not be done within the resource limitations of this effort. A further method was researched that will allow the simulation to be used over many meter ranges by utilizing a stepped set of local ~10 cm snapshot calculations at different ranges; these can be used to approximate propagation over the full streamer length. The simulation is based on a cylindrically symmetric computational volume that contains metallic objects (boundary conditions). The simulation is used to predict the breakdown of the spark gap electrode geometry shown in Figure 2. The spatial grid for the ionization is limited to points near the center ionized column while the electrostatic grid covers the entire problem space.

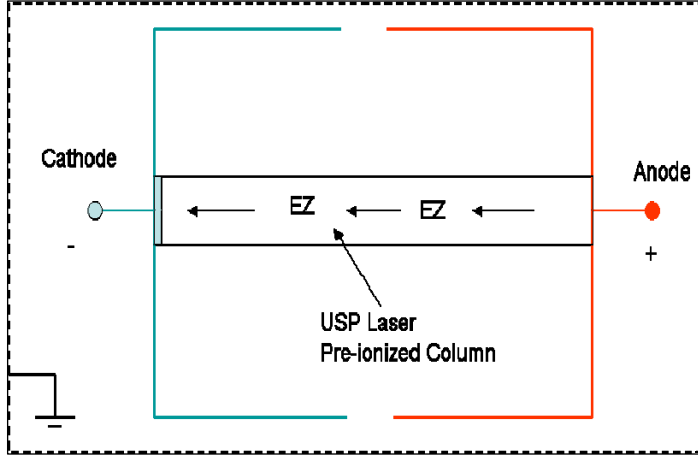


Figure 2. Simulation geometry used for numerical simulation of the electrical breakdown and ionization guided arc.

### Computational Overview

The ionized air is represented as a 5 species model

$$\begin{aligned}
 \frac{\partial n_o}{\partial t} &= -(C + B)n_e + En_m + R_{ei}n_en_+ + R_{ii}n_+n_- - S_e \\
 \frac{\partial n_e}{\partial t} + \bar{\nabla} \cdot (n_e \bar{v}_e) - D_e \nabla^2 n_e &= (C - A)n_e - R_{ei}n_en_+ + S_e \\
 \frac{\partial n_+}{\partial t} + \bar{\nabla} \cdot (n_+ \bar{v}_+) &= Cn_e - R_{ei}n_en_+ - R_{ii}n_+n_- + S_e \\
 \frac{\partial n_-}{\partial t} + \bar{\nabla} \cdot (n_- \bar{v}_-) &= An_e - R_{ii}n_+n_- \\
 \frac{\partial n_m}{\partial t} &= Bn_e - En_m
 \end{aligned} \tag{1}$$

The variables  $n_o, n_e, n_+, n_-, n_m$  refer to the neutral air, electron, positive ion, negative ion, and excited neutral molecule densities. The source terms include the Ultra-Violet (UV) ionization of the air and the cathode via the inelastic neutral molecule densities. These five equations are simultaneously solved in each finite difference cell using implicit integration techniques. The electric field is determined using a two dimensional FFT technique [Ref. 22, 23] and the electron/ion velocities are advanced using mobilities. The entire system of equations is then iterated with the circuit equations to achieve a self consistent solution with the voltage source and load impedance.

Arc formation requires the heating of the air. The macroscopic conductivity of the heated air can be used to replace the detailed microscopic treatment of charge flow at later times in the simulation. The change in specific energy of neutral air is

$$\frac{d(\rho\varepsilon)}{dt} \cong \bar{E} \cdot \bar{J} + \sigma_{ep} E^2 - \frac{4\sigma_{bb} T^4}{\ell_p}. \quad (2)$$

The temperature and electrical conductivity were then determined from Plooster's equation of state and electron mobility model [Ref. 15], [Ref. 27] given by

$$\varepsilon(\rho, T) = \left( \frac{1}{2}(5 + A_o) + 3(A_1 + A_2) \right) RT + A_o I_o + A_1 I_1 + A_2 I_2 \quad (3)$$

where  $\varepsilon$  is the specific internal energy,  $A_o$  represents the fraction of the air molecules that are dissociated and  $A_1, A_2$  represent the fraction of air atoms that have been singly or doubly ionized. These coefficients are functions of temperature  $T$  and density  $\rho$ . The electron density due to thermal ionization is given by

$$n_{ep} = 2\rho_r N_o (A_1 + A_2). \quad (4)$$

From the change in internal specific energy, it is possible to numerically solve the equation of state for temperature. The electron mobility is given by

$$\mu_{en} (m^2/V-s) \cong \frac{2.64}{\rho_r (1 - A_1) \sqrt{T(K)}} \cong \frac{2.45 \times 10^{-2}}{\rho_r (1 - A_1) \sqrt{T_{ev}}}. \quad (5)$$

The use of Plooster's equation of state eliminates the requirement to solve a potentially very large (~100) system of air chemistry equations.

### Poisson Computation Timing

The electric field solution time is dominated by the solution of Poisson's equation that finds a quasi-static field solution due to a distribution of charged particles. The fast Poisson solver that we have developed fits the grid with splines in one (radial) dimension and transforms the other free dimension ( $z$ ) via a sine transform to rapidly solve the differential equation in the "frequency domain" followed by an inverse transform back to the original spatial domain. The dominant sub-computation in the solution of the electric field is the forward and inverse sine transforms. The procedure for parallelizing FFTs is well-documented [Ref. 28].

Figure 3 shows computational timing results comparing the FFT-based fast Poisson solver, developed for this simulation, to a Successive Over-Relaxation (SOR) method. For this test case, the potential is solved for a conducting sphere at the origin of a square computational grid.

The red curve shows the computation time for the fast solver; the blue the computation time for the SOR method; each as a function of grid size. The pink and green lines are present merely to guide the eye: they approximately match the curves at the first point and show the expected times for algorithms that scale as the square of the linear dimension. That is, they show an ideal scaling for a problem that grows in proportion to the number of cells. The fast FFT method does a reasonable job at following the curve up until the last point (8196 points) where, most likely, the size of the arrays exceed the cache of the processor and an additional time is required due to swap memory in and out of the CPU. If the supposition is true, the problem should be negated by our proposed parallel approach. The time of the SOR computation grows so quickly that it did not make sense to compute a solution for a grid larger than 1024 by 1024.

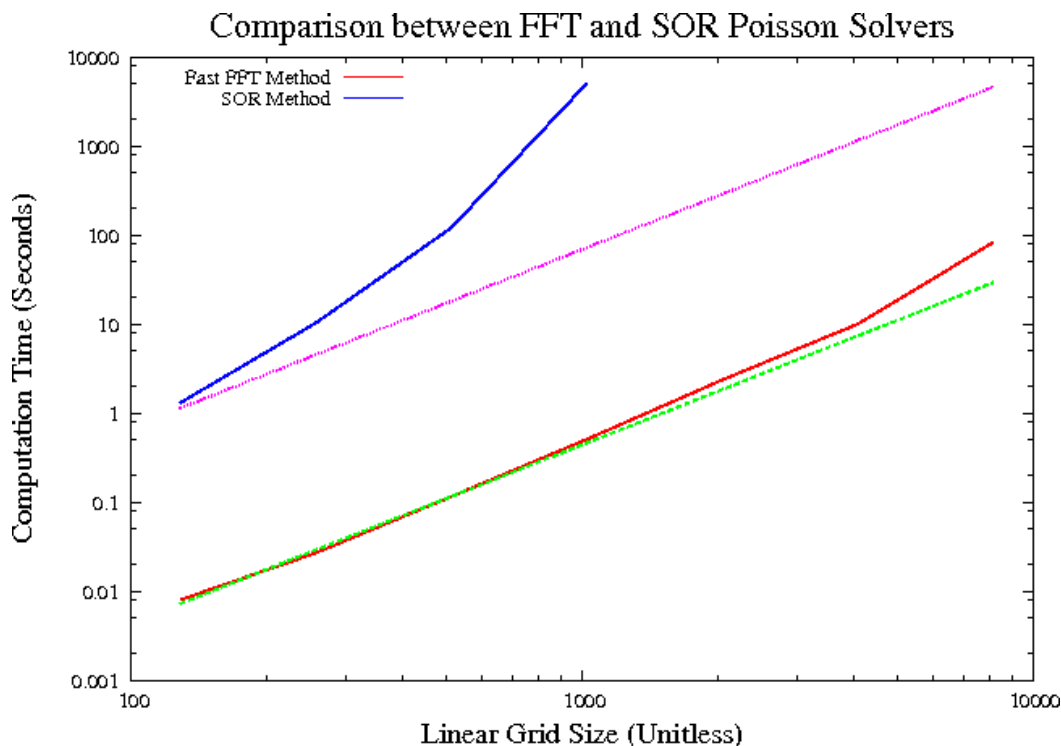


Figure 3. Timing Comparison of FFT and SOR Based Methods.

### Considerations for Utilizing Parallel Processing

Though beyond the resources of the current effort the mechanics of performing the conversion to parallel processing have been studied and outlined. This extension can be accomplished using the standard Message Passing Interface (MPI.) In particular, the Local Area Multicomputer-Message Passing Interface (LAM/MPI) can use the MPI implementation [Ref. 29]. MPI provides Fortran and C routines that allow easy and safe communication between processors. To model electrical breakdown for geometries where the electrons are separated by a meter or more it will be necessary to break the problem up into a series of smaller snapshots. Each snapshot will model the streamer head over dimensions of approximately 10 cm at various locations

between the cathode and the anode. If the discharge is seen to propagate for each snapshot then clearly the discharge will propagate from the cathode to the anode. A similar approach has been used for the Nuclear Lightning problem [Ref.21]. This process is illustrated in Figure 4. The left hand part of the Figure shows the relationship between the larger finite difference spatial grid, where the electrostatic solution is solved, and one particular location of the sub-grid where the rate equations are advanced. The USP induced ionization channel is located along the axis between the cathode and the anode and the discharge moves from bottom to top in Figure 4. below. The sub-grid, the electrical discharge is known to be a hot leader below. As such it must have a relatively high electrical conductivity and its potential is, therefore, set to the same potential as the cathode. The right hand part of the Figure shows the propagation of the electrical discharge within the sub-grid. The decision as to whether the discharge is propagating through the sub-grid is straightforward. If the shape and velocity of the tip of the discharge is the same at two times along the path, say  $T_{start}$  and  $T_{stop}$ , then the discharge is propagating and not dissipating. In that case, the projected discharge path over the entire extent of the sub-grid is set to the electrical conductivity of the hot leader and the location of the rate equation sub-grid is moved up by approximately 10 cm along the discharge path as the leader propagates. This process may be repeated over the entire cathode anode separation path so that the sub-grid is co-located with the tip of the leader.

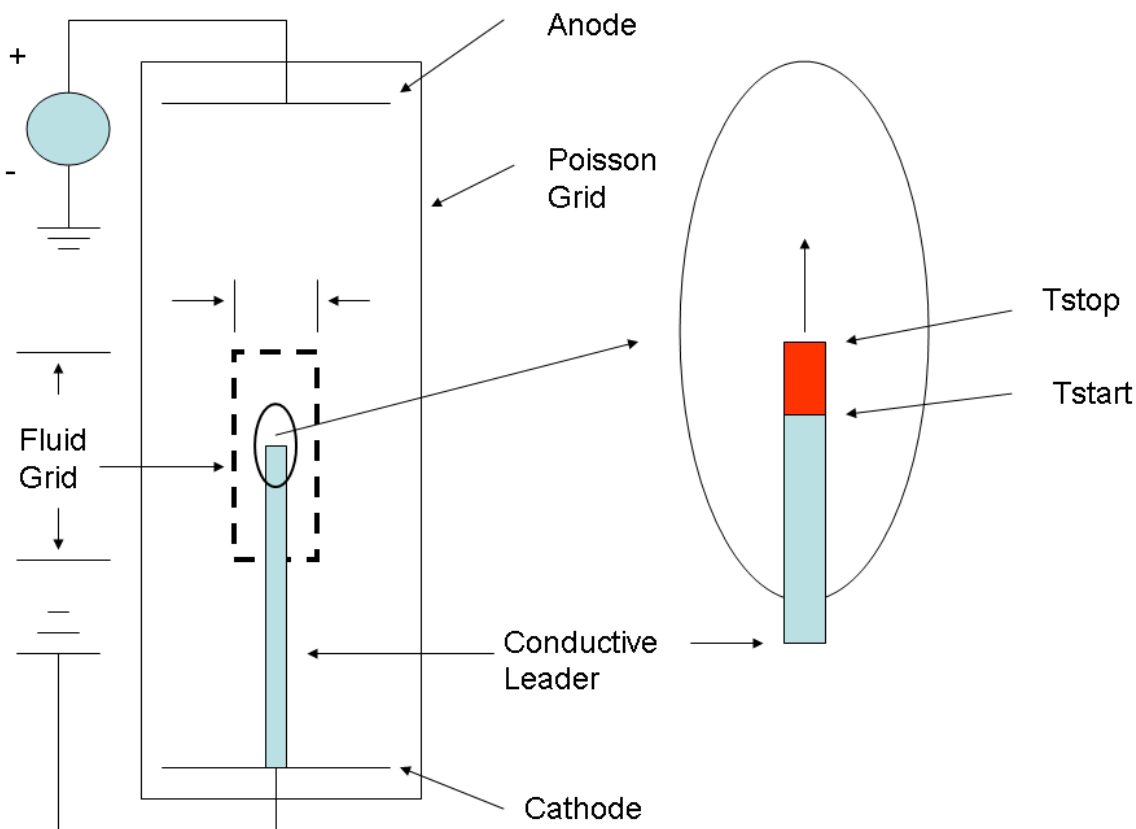


Figure 4. Scheme for implementing a snapshot calculation for extended ranges.

## 2.0 Theoretical Formulation

The fluid approach for electrons can be carried out by equilibrium or a non-equilibrium model. In both cases the quantities of interest are the number densities and the drift velocities. In the equilibrium model it is assumed that the acceleration due to the local electric field is balanced by the collision rate and so the drift velocity is a function of the local electric field. However it is not assumed that the electrons and ions/neutrals have the same temperature and during the initial breakdown-streamer phase we expect that the electron temperature is significantly higher than the ion/neutral temperature i.e.  $T_e \gg T_i, T_o$ . In the non-equilibrium model the drift velocity is determined by solving the fluid equation for momentum. In the equilibrium model we need the continuity equation for the electrons and ion species, electric field mobilities to relate the electron and ion velocities to the local electric field, and electric field dependent rate coefficients for the various processes that add and subtract to the various number densities. In the non-equilibrium model we need continuity equations for number density, momentum, and energy density, as well as an equation of state. In this case the rate coefficients are typically written in terms of energy.

Although the non-equilibrium approach offers a more detailed description of the breakdown dynamics the solution of the fluid equations adds considerable complexity to the problem. Therefore the equilibrium approach will be initially followed. The fluid equations needed for the non-equilibrium approach are separately documented.

### Equilibrium Model

The equilibrium model for the electron and ion species is given by a set of continuity equations i.e.

$$\begin{aligned}
 \frac{\partial n_o}{\partial t} &= Sources - Sinks \\
 \frac{\partial n_e}{\partial t} + \bar{\nabla} \cdot (n_e \bar{v}_e) - D_e \nabla^2 n_e &= Sources - Sinks \\
 \frac{\partial n_+}{\partial t} + \bar{\nabla} \cdot (n_+ \bar{v}_+) &= Sources - Sinks \\
 \frac{\partial n_-}{\partial t} + \bar{\nabla} \cdot (n_- \bar{v}_-) &= Sources - Sinks \\
 \frac{\partial n_m}{\partial t} &= Sources - Sinks.
 \end{aligned} \tag{6}$$

plus a set of mobility equations

$$\begin{aligned}
\bar{v}_e &= -\mu_e \left( |\bar{E}| \right) \bar{E} \\
\bar{v}_+ &= \mu_p \left( |\bar{E}| \right) \bar{E} \\
\bar{v}_- &= -\mu_p \left( |\bar{E}| \right) \bar{E}.
\end{aligned} \tag{7}$$

In the continuity equations  $n_o$  is the number density of neutral molecules in the ground state,  $n_e$  is the number density of electrons,  $n_+$  is the number density of singly charged ions,  $n_-$  is the number of negatively charged ions, and  $n_m$  is the number density of neutral molecules in an average excited state. In general the source and sink terms can have an arbitrarily large number of cross coupling terms. Note that we are dropping the divergence term for the neutral molecules and the diffusion term for all the ion species.

The various processes contained in the source and sink terms include electron avalanche, electron attachment, electron-ion and ion-ion recombination, inelastic excitation and decay of neutral molecules, and photo-ionization of neutral molecules. As a result we can rewrite the continuity equations

$$\begin{aligned}
\frac{\partial n_o}{\partial t} &= -(C + B)n_e + En_m + R_{ei}n_en_+ + R_{ii}n_+n_- - S_e \\
\frac{\partial n_e}{\partial t} + \bar{\nabla} \cdot (n_e \bar{v}_e) - D_e \nabla^2 n_e &= (C - A)n_e - R_{ei}n_en_+ + S_e \\
\frac{\partial n_+}{\partial t} + \bar{\nabla} \cdot (n_+ \bar{v}_+) &= Cn_e - R_{ei}n_en_+ - R_{ii}n_+n_- + S_e \\
\frac{\partial n_-}{\partial t} + \bar{\nabla} \cdot (n_- \bar{v}_-) &= An_e - R_{ii}n_+n_- \\
\frac{\partial n_m}{\partial t} &= Bn_e - En_m.
\end{aligned} \tag{8}$$

These equations can be written in the general form

$$\frac{dn_i}{dt} = \sum_k a_i(j)n_k + \sum_j \sum_k b_i(j,k)n_jn_k + \dots - \bar{\nabla} \cdot (n_i \bar{v}_i) + S_i. \tag{9}$$

We can define an early and a late time regime for the calculations. The early time regime models the propagation of the avalanche and streamer. At late times when the electron avalanche has crossed the gap between the two electrodes the problem should settle to a steady state where the gradients of the electron and ion densities become relatively constant in time. At this point the divergence term in the above equation becomes relatively unimportant and can be dropped. The resulting system of ordinary differential equations can now be advanced with a much larger time step. This later regime will be called the late time regime and is characterized by the transition to an arc.

We now need to specify the various terms in these equations. We will begin with the mobility terms.



## Electron and Ion Mobility

The drift velocity of electrons at equilibrium is found from

$$\frac{d\bar{v}_e}{dt} = \frac{e}{m_e} \bar{E} - \nu_e^m \bar{v}_e = 0 \quad (10)$$

resulting in

$$\bar{v}_e = \frac{e}{m} \frac{1}{\nu_e^m} \bar{E} = \mu_e \bar{E} . \quad (11)$$

We will assume that the ionization level is low enough so that only collisions with neutral molecules need to be considered and so

$$\mu_e = \frac{e}{m} \frac{1}{\nu_{eo}^m} = \frac{e}{m} \frac{1}{n_o \langle \sigma_m w_e \rangle} . \quad (12)$$

From Kline [Ref. 1] we find

$$\mu_e (cm^2 / V - s) \cong 2.7 \times 10^5 / P(Torr) . \quad (13)$$

From Vitello [Ref. 7] we find

$$\begin{aligned} \mu_e (cm^2 / V - s) &\cong 2.9 \times 10^5 / P(Torr) \\ \mu_p (cm^2 / V - s) &\cong 2.6 \times 10^3 / P(Torr) \end{aligned} . \quad (14)$$

The assumption that the drift velocity is proportional to electric field strength breaks down for both high electric field strengths and high ionization densities. Longmire [Ref. 30] gives

$$\mu_e \rho_r (m^2 / V - s) \cong \begin{cases} 0.79 & , E / \rho_r < 3 \times 10^3 V / m \\ 0.25 \sqrt{3 \times 10^4 \rho_r / E} & , 3 \times 10^3 < E / \rho_r < 3 \times 10^5 V / m \\ 0.079 & , E / \rho_r > 3 \times 10^5 V / m \end{cases} \quad (15)$$

where the relative air density defined at low pressure is  $\rho_r = n_o / N_o$ . We will further assume that  $\rho_r$  is fixed by the initial conditions, consistent with the weak ionization assumption used here. Vitello's result for the electron drift velocity in nitrogen should also be modified for high field levels. A possible modification is (MKS units)

$$\mu_e \rho_r (m^2 / V - s) \cong \begin{cases} 3.8 \times 10^{-2} & , E / \rho_r < 1.14 \times 10^7 V / m \\ 3.8 \times 10^{-2} \sqrt{1.14 \times 10^7 \rho_r / E(V / m)} & , E / \rho_r \geq 1.14 \times 10^7 V / m \end{cases} \quad (16)$$

We will use the last two results for the electron mobility in air and nitrogen respectively. For the ion mobility we will use values for air and nitrogen from Longmire [Ref. 28] and Vitello i.e.

$$\begin{aligned} \mu_p \rho_r (cm^2 / V - s) &\cong 2.4 \times 10^{-4} - Air \\ \mu_p \rho_r (cm^2 / V - s) &\cong 3.4 \times 10^{-4} - Nitrogen \end{aligned} \quad (17)$$

### Electron Diffusion

From Vitello we get in MKS units

$$D_e \rho_r (m^2 / s) \cong 0.2. \quad (18)$$

### Electron Collision Ionization

The electron impact ionization or first Townsend coefficient is also given by Vitello

$$\begin{aligned} \alpha (m^{-1}) &= 570 P(Torr) \exp \left( \frac{-26000 P(Torr)}{E(V / m)} \right) \\ &= 4.33 \times 10^5 \rho_r \exp \left( \frac{-1.98 \times 10^7}{E(V / m) / \rho_r} \right) \end{aligned} \quad (19)$$

We can now form the electron avalanche or cascade rate as the product of the first Townsend coefficient and the electron drift velocity. We have

$$\begin{aligned} C (sec^{-1}) &= \alpha (m^{-1}) |\bar{v}_e| (m / sec) \\ &= 4.33 \times 10^5 \rho_r \exp \left( \frac{-1.98 \times 10^7}{E(V / m) / \rho_r} \right) \mu_e |\bar{E}|. \end{aligned} \quad (20)$$

### Inelastic Excitation and Decay

The macroscopic cross section  $\delta (cm^{-1})$  for inelastic excitation of neutral molecules is given as a ratio  $\delta / \alpha$  by Yoshida [Ref.4] as

$$\frac{\delta}{\alpha} = \left( \frac{\delta_o}{\alpha} \right) [1 + (P/P_o)]^{-1}$$

$$\frac{\delta_o}{\alpha} = 0.101 + \frac{268}{(E/P)} - \frac{353.4 \times 10^2}{(E/P)^2} + \frac{547.3 \times 10^4}{(E/P)^3} - \frac{160.5 \times 10^6}{(E/P)^4} + \frac{212.4 \times 10^7}{(E/P)^5} \quad (21)$$

where  $P_o \cong 60 \text{ Torr}$  is the quenching pressure of the inelastic transition of interest. The decay time of the transition is also given by Yoshida

$$\tau_m = \frac{\tau_o}{1 + P/P_o} \quad (22)$$

where  $\tau_o \cong 36 \text{ ns}$  is the low pressure value. To be consistent we will use from Yoshida

$$\alpha (cm^{-1}) = 7.56 P(Torr) \exp\left(\frac{-272}{E/P}\right). \quad (23)$$

In the above equations  $E/P$  has units of volts/cm-Torr. We can now define the rate coefficient for creation of excited neutral molecules by

$$B(sec^{-1}) = \delta(m^{-1}) |\bar{v}_e| (m/sec). \quad (24)$$

The rate coefficient for decay of the excited molecules is given by

$$E(sec^{-1}) = \frac{1}{\tau_m}. \quad (25)$$

### Electron Attachment

For the electron attachment rate in air we will use the simple three body rate from Longmire [Ref. 31]

$$A(sec^{-1}) \cong 10^8 \rho_r^2. \quad (26)$$

The difference between attachment and avalanche ( $C - A$ ) will determine the electron avalanche/breakdown threshold in air.

### *Electron-Ion Recombination*

he electron-ion reaction is assumed to go by radiative recombination and can be approximated from Longmire as

$$R_{ei} = 2 \times 10^{-13} \quad . \quad (27)$$

### *Ion-Ion Recombination*

The ion-ion recombination reaction is assumed to be a three body mechanism and can be approximated from Longmire as

$$R_{ii} (m^3 / s) = 2 \times 10^{-12} \rho_r. \quad (28)$$

### UV Photo-Ionization

In order to complete the model we need to consider photo-ionization of the ambient gas and electron photoemission from the cathode.

Given the source  $S_p$  (photons /  $cm^3$  – sec) the ionization rate at a location  $\bar{R} = \bar{0}$  is given by

$$S_e = \iiint_{\text{all space}} \frac{\eta S_p(\bar{R}') \mu_a e^{-\mu_a R'}}{4\pi R'^2} dV \quad (29)$$

or as given by Penny [Ref. 6]

$$S_e = \iiint_{\text{all space}} \frac{\dot{n}_D(\bar{R}') \psi(R'P) P dV}{4\pi R'^2}. \quad (30)$$

Penny has semi log plots of  $\psi(RP)$  vs  $x = RP$  for nitrogen and air. In order to use these results here the coefficient  $\psi(x)$  was fit by a sum of exponentials of the form

$$\psi(x) = a_1 e^{-b_1 x} + a_2 e^{-b_2 x} + \dots \quad (31)$$

where  $x$  is the range in units of cm-Torr. A simple fitting procedure was used where the plot was divided up into sections and each section was fit by a single exponential using the relations

$$b_1 = \frac{\ln(\psi_1) - \ln(\psi_2)}{x_2 - x_1} \quad (32)$$

$$a_1 = \psi_2 / e^{-b_1 x}.$$

For air we have a three term fit where

$$\begin{aligned} a_1 &= 5.0 \times 10^{-4} & b_1 &= 2.705 \times 10^{-1} \\ a_2 &= 6.0 \times 10^{-6} & b_2 &= 1.455 \times 10^{-2} \\ a_3 &= 6.0 \times 10^{-7} & b_3 &= 6.383 \times 10^{-3}. \end{aligned} \quad (33)$$

For nitrogen we have a three term fit where

$$\begin{aligned} a_1 &= 1.0 \times 10^{-3} & b_1 &= 3.838 \times 10^{-1} \\ a_2 &= 3.0 \times 10^{-7} & b_2 &= 2.906 \times 10^{-2} \\ a_3 &= 2.0 \times 10^{-8} & b_3 &= 2.302 \times 10^{-3}. \end{aligned} \quad (34)$$

A list is given in Table 1 which gives the values for the empirical coefficient  $\psi(RP)$  with units of electron-ion pairs created per ionizing collision-str-cm-Torr as a function of the range-pressure product. Also shown is the effective photon absorption coefficient  $\mu(cm^{-1}Torr^{-1})$  for air and nitrogen.

Table 1.  
Ionization and Absorption Coefficients

$RP(cm-Torr)$	$\psi(air)$	$\psi(nitrogen)$	$\mu(air)$	$\mu(nitrogen)$
1.000E+01	3.919E-05	2.178E-05	6.331E-02	2.239E-01
4.105E+01	3.771E-06	1.093E-07	2.463E-02	3.331E-02
7.211E+01	2.480E-06	5.385E-08	1.903E-02	1.558E-02
1.032E+02	1.648E-06	3.074E-08	1.623E-02	9.611E-03
1.342E+02	1.106E-06	2.076E-08	1.446E-02	6.739E-03
1.653E+02	7.508E-07	1.613E-08	1.319E-02	5.089E-03
1.963E+02	5.162E-07	1.373E-08	1.224E-02	4.034E-03
2.274E+02	3.600E-07	1.226E-08	1.147E-02	3.309E-03
2.584E+02	2.550E-07	1.120E-08	1.085E-02	2.784E-03
2.895E+02	1.835E-07	1.034E-08	1.032E-02	2.389E-03
3.205E+02	1.341E-07	9.590E-09	9.872E-03	2.082E-03
3.516E+02	9.963E-08	8.914E-09	9.481E-03	1.838E-03
3.826E+02	7.510E-08	8.293E-09	9.136E-03	1.640E-03
4.137E+02	5.738E-08	7.719E-09	8.829E-03	1.476E-03
4.447E+02	4.439E-08	7.185E-09	8.554E-03	1.339E-03
4.758E+02	3.470E-08	6.689E-09	8.305E-03	1.222E-03
5.068E+02	2.737E-08	6.228E-09	8.079E-03	1.122E-03
5.379E+02	2.176E-08	5.798E-09	7.872E-03	1.036E-03
5.689E+02	1.741E-08	5.398E-09	7.681E-03	9.602E-04
6.000E+02	1.400E-08	5.026E-09	7.504E-03	8.938E-04

### UV Photo-Emission

In order to determine the electrical discharge UV induced photoemission at the cathode we need the incident directed photon flux at the cathode surface. This flux is given by

$$Q_p^+ = \iiint_{\text{half space}} \frac{(\hat{e}_n \cdot \hat{\Omega}) S_p(\bar{R}') e^{-\mu_a R'} dV}{4\pi R'^2} \quad (35)$$

where  $\hat{e}_n$  is the unit normal to the cathode surface and  $\hat{\Omega}$  is the element of solid angle. Again it is interesting to consider the case where  $S_p(\bar{R}')$  is uniform over the half space. Rewriting in spherical coordinates we have

$$\begin{aligned} Q_p^+ &= \int_{R'=0}^{R'=\infty} \int_{\theta=0}^{\theta=\pi} \int_{\phi=0}^{\phi=2\pi} \frac{\cos \theta S_p e^{-\mu_a R'} R'^2 dR' \sin \theta d\theta d\phi}{4\pi R'^2} \\ &= \frac{S_p}{4} \int_{R'=0}^{R'=\infty} e^{-\mu_a R'} dR' = \frac{S_p}{4\mu_a}. \end{aligned} \quad (36)$$

The resulting one-sided electron flux is given by

$$\Gamma^+(e/cm^2 - \text{sec}) = Y_p(e/p) Q_p^+(p/cm^2 - \text{sec}). \quad (37)$$

Explicitly putting in the pressure term results in, [Ref. 4] [Yoshida, (1), (2) 71],

$$\Gamma_e^+ = \iiint_{\text{half space}} \frac{Y_p(\hat{e}_n \cdot \hat{\Omega}) S_p(\bar{R}') e^{-(\mu_a/P)R'P} dV}{4\pi R'^2}. \quad (38)$$

The advantage of this formulation is that the pressure normalized absorption coefficient  $\mu_a/P$  can be derived from experiment. However we will still need to find the photon source term  $S_p(\bar{R}')$  and the cathode electron yield coefficient  $Y_p(e/p)$ .

Penny [Ref.2] has provided log-log plots of  $\mu(x) = \mu_a/P$  for nitrogen and air. In order to use their results here the coefficient  $\psi(x)$  was fit by a power sum

$$\mu(x) = a_1 x^{-b_1} + a_2 x^{-b_2} + \dots \quad (39)$$

where  $\mu$  has units of cm<sup>-1</sup> torr<sup>-1</sup> and  $x$  is the range in units of cm-Torr. A simple fitting procedure was used where the plot was divided up into sections and each section was fit by a single exponential using the relations

$$\begin{aligned} b_1 &= \frac{\ln(\mu_1) - \ln(\mu_2)}{\ln(x_2) - \ln(x_1)} \\ a_1 &= \mu_2(x) / x_2^{-b_1}. \end{aligned} \quad (40)$$

For air we have a two term fit where

$$\begin{aligned} a_1 &= 10.0 & b_1 &= 2.736 \\ a_2 &= 0.123 & b_2 &= 0.4372. \end{aligned} \quad (41)$$

For nitrogen we have a one term fit where

$$a_1 = 5.0 \quad b_1 = 1.349. \quad (42)$$

A list of values is also given in Table 1.

As discussed previously the photon source is given by

$$S_p = \frac{n_m}{\tau_m}. \quad (43)$$

From Yoshida [Ref. 4] we find that the cathode electron yield is related to the first Townsend coefficient  $\alpha(cm^{-1})$ , the inelastic excitation coefficient  $\delta(cm^{-1})$  (macroscopic cross section for electron collision induced inelastic excitations of neutral molecule states that then decay by photoemission), and the second Townsend coefficient  $\gamma$  by the relationship

$$\delta Y_p = \alpha \gamma. \quad (44)$$

The second Townsend coefficient  $\gamma$  is a function of the cathode material, the ambient gas, and the electric field to pressure ratio  $E/P$  and is defined as the number of secondary electrons produced at the cathode per ion pair produced in the gas. Values typically vary between  $10^{-1}$  and  $10^{-3}$ . The first and second Townsend coefficients are combined to give the simple electrical breakdown criteria for small gaps i.e.

$$\gamma e^{\alpha d} = 1. \quad (45)$$

For electrical discharges in nitrogen at  $P=300$  Torr Yoshida also suggests a value  $\gamma \sim 8.2 \times 10^{-3}$ . The ratio  $\delta/\alpha$  was discussed previously. Values for  $\alpha/P$ ,  $\alpha$ ,  $\delta/\alpha$ , and  $\delta$  are given in Table 2. For reference  $5MV/m$  at 760 Torr corresponds to 66 V/cm-Torr. Choosing  $E/P = 50V/cm-Torr$  results in  $\delta/\alpha \cong 1.19$  and

$$Y_p(e/p) = \left( \frac{\alpha}{\delta} \right) \gamma = \left( \frac{1}{1.19} \right) (8.2 \times 10^{-3}) \sim 1 \times 10^{-2}. \quad (46)$$

This result is somewhat higher than values of  $10^{-3} - 10^{-4}$  anticipated from some unpublished data taken by one of the authors on unprepared samples of copper.

Table 2 gives values for  $\alpha / P(cm^{-1}Torr^{-1})$ ,  $\alpha(cm^{-1})$ ,  $\delta / \alpha$  and  $\delta(cm^{-1})$  [Yoshida, (1), (2), 76] as a function of  $E / P (V / cm - Torr)$  at a pressure of 760 Torr. The decay time for the level is  $\tau \cong 2.63ns$ .

Table 2  
Electrical Coefficients for Air

$\frac{E}{P}(V/cm-T)$	$\frac{\alpha}{P}(cm^{-1}Torr^{-1})$	$\alpha(cm^{-1})$	$\delta / \alpha$	$\delta(cm^{-1})$
1.000E+01	1.163E-11	8.841E-09	7.563E+02	6.687E-06
2.000E+01	9.378E-06	7.127E-03	1.975E+01	1.408E-01
3.000E+01	8.728E-04	6.633E-01	4.517E+00	2.996E+00
4.000E+01	8.420E-03	6.399E+00	2.069E+00	1.324E+01
5.000E+01	3.281E-02	2.493E+01	1.187E+00	2.960E+01
6.000E+01	8.123E-02	6.174E+01	7.636E-01	4.714E+01
7.000E+01	1.552E-01	1.180E+02	5.307E-01	6.261E+01
8.000E+01	2.523E-01	1.917E+02	3.913E-01	7.504E+01
9.000E+01	3.681E-01	2.798E+02	3.027E-01	8.468E+01
1.000E+02	4.980E-01	3.785E+02	2.435E-01	9.215E+01

### Air Heating Model

The early time equilibrium streamer dynamics assume that the electron temperature is directly related to the local electric field and air density. In fact, the molecular gas will heat up from electron-neutral collisions. If we consider the contributions due to Joule heating from electron and ion currents

$$\bar{J} = e(n_e \bar{v}_e + \sum n_- \bar{v}_-) + |e| \sum n_+ \bar{v}_+ \quad (47)$$

and an additional term from the intrinsic thermally induced electrical conductivity  $\sigma_{pe}$  of the neutral gas we can calculate the change of internal energy from

$$\frac{d(\rho \varepsilon)}{dt} \cong \bar{E} \cdot \bar{J} + \sigma_{ep} E^2 - \frac{4\sigma_{bb} T^4}{\ell_p} \quad (48)$$

where  $\varepsilon$  is the specific internal energy. The last term in the above equation represents the radiative loss of energy from an optically thin gas where  $\sigma_{bb} \cong 5.67 \times 10^{-8} W / m^2 - deg K^4$ . The Plank mean free path  $\ell_p$  was not available so the Rosseland mean free path  $\ell_R \sim 10m$  at a temperature of 10,000 degrees K was used Brode [Ref. 32]. For the present time we will ignore hydrodynamic effects and assume that the gas density is constant so  $\rho_0 = 1.17688 \text{ kg/m}^3$



$$\frac{d\varepsilon}{dt} \cong \frac{1}{\rho_o} \left( \bar{E} \cdot \bar{J} + \sigma_{pe} E^2 - \frac{4\sigma_{bb} T^4}{\ell_R} \right). \quad (49)$$

A relatively simple model for the electrical conductivity of heated air has been proposed by Plooster [Ref. 27] that consists of a caloric equation of state that can be inverted to get the temperature as a function of specific energy density and an electrical conductivity model. Plooster's equation of state is written

$$\varepsilon(\rho, T) = \left( \frac{1}{2}(5 + A_o) + 3(A_1 + A_2) \right) RT + A_o I_o + A_1 I_1 + A_2 I_2 \quad (50)$$

where  $\varepsilon$  is the specific internal energy,  $A_o$  represents the fraction of the air molecules that are dissociated, and  $A_1, A_2$  represents the fraction of air atoms that have been singly or doubly ionized. These coefficients are functions of temperature  $T$ , and density  $\rho$ . The electron density due to thermal ionization is given by

$$n_{ep} = 2\rho_r N_o (A_1 + A_2). \quad (51)$$

Given the change in internal specific energy it is possible to numerically solve the equation of state for temperature. Then the electron-neutral and electron-ion mobilities are given by

$$\mu_{en} (m^2 / V - s) \cong \frac{2.64}{\rho_r (1 - A_1) \sqrt{T(K)}} \cong \frac{2.45 \times 10^{-2}}{\rho_r (1 - A_1) \sqrt{T_{eV}}} \quad (52)$$

and

$$\mu_{ei} (m^2 / V - s) \cong \frac{1.89 \times 10^{-9} T(K)^{3/2}}{\rho_r A_1 \ln \left( \frac{1.63 \times 10^{-4} T(K)}{(A_1 \rho_r)^{1/3}} \right)} \cong \frac{2.36 \times 10^{-3} T_{eV}^{3/2}}{\rho_r A_1 \ln \left( \frac{1.89 T_{eV}}{(A_1 \rho_r)^{1/3}} \right)}. \quad (53)$$

The electron-neutral and electron-ion conductivities are given by

$$\begin{aligned} \sigma_{enp} &= |e| n_{ep} \mu_{enp} = F_1(n_{ep}, T) \\ \sigma_{eip} &= |e| n_{ep} \mu_{eip} = F_2(n_{ep}, T) \end{aligned} \quad (54)$$

and the resulting conductivity is given by

$$\sigma_{ep} = \frac{\sigma_{en} \sigma_{ei}}{\sigma_{en} + \sigma_{ei}}. \quad (55)$$

## Electrostatic Model

In addition to creating and transporting charge it is necessary to advance the electric fields in a self-consistent manner. The approach used here is to advance Poisson's equation

$$\nabla^2 \phi = \frac{\partial^2 \phi}{\partial r^2} + \frac{1}{r} \frac{\partial \phi}{\partial r} + \frac{\partial^2 \phi}{\partial z^2} = -\frac{\rho}{\epsilon_o} \quad (56)$$

where the net charge density at the corners of the finite difference cell are determined by summing the free electrons, positive ions and negative ions i.e.

$$\rho = e \left( n_e + \sum n_- \right) + |e| \sum n_+. \quad (57)$$

The electric field is then found from  $\bar{E} = -\nabla \phi$ . Solving Poisson's equation also requires the electron boundary conditions. For the early time discharge we will define an effective discharge current

$$I_d = \int_{Z_l}^{Z_u} \left( \int_0^R J_z 2\pi r dr \right) dz / \int_{Z_l}^{Z_u} dz. \quad (58)$$

The voltage drop across the electrodes is then given by  $V_u - V_l = V_s - I_d R_s$

### 3.0 Numerical Formulation

The coordinate system is shown in Figure 5. The outer boundaries are defined on the lower, upper, and outer surfaces by boundary potentials  $VL, VU, VO$ .

$$\begin{aligned}\phi(i,1) &= VL \\ \phi(i,nez) &= VU \\ \phi(ner,k) &= VO.\end{aligned}\tag{59}$$

The object potentials  $V_i$  (pot\_modmap(i,k)) are also set along with any fixed charge  $\rho_{fixed}(i,k)$  and the volume charge  $\rho(i,k)$  is set to zero. A direct solution technique described by Kunhardt [Ref. 25], and Hockney [Ref. 26] was adapted. We begin by with Poisson's equation

$$\nabla^2 \phi = \frac{\partial^2 \phi}{\partial r^2} + \frac{1}{r} \frac{\partial \phi}{\partial r} + \frac{\partial^2 \phi}{\partial z^2} = -\frac{\rho}{\epsilon_o}\tag{60}$$

and expand the potential and charge density as discrete sine transforms in the  $z$  direction

$$\begin{aligned}\phi(r,z) &= \sum_{n=1}^{\infty} \phi_n(r) \sin\left(\frac{n\pi z}{Z_{\max}}\right) \\ \rho(r,z) &= \sum_{n=1}^{\infty} \rho_n(r) \sin\left(\frac{n\pi z}{Z_{\max}}\right).\end{aligned}\tag{62}$$

Note that this expansion assumes that the potential is zero at the lower and upper outer boundaries. This is not really a limitation as we can place inner surfaces of arbitrary potential to build the desired problem. Using this approach along with the assumption of a uniform mesh in the axial or  $z$  directions it can be shown that

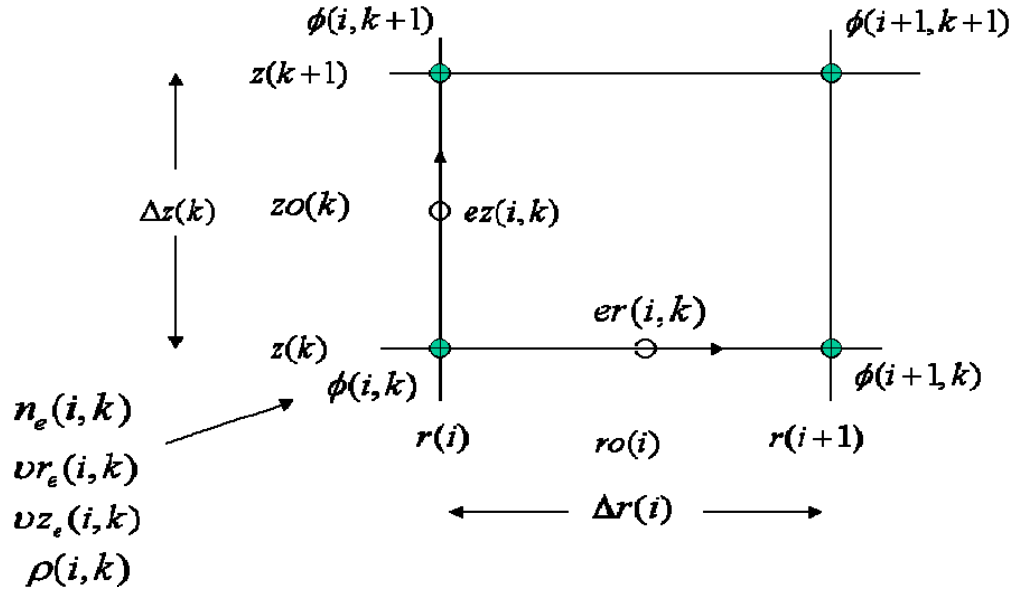


Figure 5. Numerical grid for the two dimensional problem.

(63)

$$\frac{\partial^2 \phi_n(r)}{\partial^2 r} + \frac{1}{r} \frac{\partial \phi_n(r)}{\partial r} + \frac{2}{\Delta z^2} \left[ \cos\left(\frac{n\pi}{N_z+1}\right) - 1 \right] \phi_n(r) = \frac{-\rho_n(r)}{\epsilon_o}. \quad (64)$$

This equation is tridiagonal on the 2D finite difference mesh. The method of solution is as follows. First the quantities  $\rho_n(r)$  are determined by fast sine transforms as described by Press et al [Ref. 33]. Then we solve the tridiagonal equation shown above for  $\phi_n(r)$ . Finally we find the potential on the two dimensional mesh by the fast sine transform.

$$\phi(r, z) = \sum_{n=1}^{\infty} \phi_n(r) \sin\left(\frac{n\pi z}{Z_{\max}}\right). \quad (65)$$

In order to use this direct approach it is necessary to convert the electrical potential of defined objects or surfaces within the grid to equivalent electrical charges. First consider an interior potential surface as shown in Figure 6.

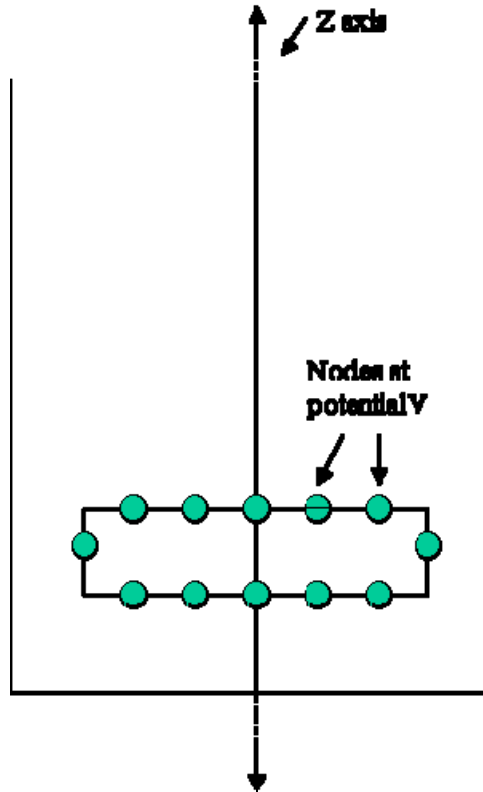


Figure 6. Placement of a potential surface in the finite difference grid.

We begin by placing a unit charge ( $q_1 = 1/\epsilon_o$ ) at the first object node on the potential surface and solve Poisson's equation using the direct solver to find the potentials at all the nodes on the potential surface. We then set

$$\begin{aligned} a_{11} &= V_1 \\ a_{21} &= V_2 \\ &\dots\dots\dots \\ a_{n1} &= V_n. \end{aligned} \tag{66}$$

We then repeat this process for the rest of the nodes and form a system of equations which relates the potentials at the object nodes to the charges at the nodes i.e.

$$\begin{bmatrix} V_1 \\ V_2 \\ \vdots \\ V_n \end{bmatrix} = \begin{bmatrix} a_{11} & a_{12} & \cdot & a_{1n} \\ a_{21} & a_{22} & \cdot & a_{2n} \\ \cdot & \cdot & \cdot & \cdot \\ a_{n1} & a_{n2} & \cdot & a_{nn} \end{bmatrix} \begin{bmatrix} q_1 \\ q_2 \\ \cdot \\ q_n \end{bmatrix} \tag{67}$$

or

$$\bar{V} = \bar{\bar{C}}^{-1} \bar{q}. \tag{68}$$

As a result by calling the direct solver  $n$  times we can form the inverse capacitance matrix  $\bar{\bar{C}}^{-1}$ . This matrix is normally not excessively large and can be inverted to get the capacitance matrix  $\bar{\bar{C}}$ . This operation only has to be done at the beginning of the calculation and only if the geometry changes. The spark code checks to see if the capacitance matrix needs to be recalculated at the beginning of each run.

Given the capacitance matrix the Poisson calculation proceeds as follows. First the direct solver solves for the potentials given the ionization charge but ignoring the boundaries. The resulting (false) potentials  $\bar{V}^*$  at the object nodes are then used to calculate false charges via

$$\bar{q}^* = \bar{\bar{C}} \bar{V}^*. \tag{69}$$

Then the negative of the false charges is added to the ionization charge and the direct solver again solves for the potentials. At this point all the potentials at the object surface are zero. If the object potentials are not zero we only need to subtract them from  $\bar{V}^*$  and solve

$$\bar{q}^* = \bar{\bar{C}} (\bar{V} - \bar{V}_{object}). \tag{70}$$

Once the potentials are determined the initial electric fields are found from

$$\begin{aligned} er(i, k) &= -[\phi(i+1, k) - \phi(i, k)] / \Delta r(i) \\ ez(i, k) &= -[\phi(i, k+1) - \phi(i, k)] / \Delta x(k). \end{aligned} \quad (71)$$

We also need to initialize the late time Plooster equation of state variables. The only difference is adding an additional dimension to the previous results. Given the initial neutral gas temperature  $T(i, k)$  and density  $\rho_o$  we have

$$se(i, k) = \varepsilon(\rho_o, T(i, k)) \quad (72)$$

$$n_{ep}(i, k) = 2\rho_r N_o (A_1(T(i, k)) + A_2(T(i, k))) \quad (73)$$

$$\begin{aligned} \sigma_{enp}(i, k) &= F_1(n_{ep}(i, k), T(i, k)) \\ \sigma_{eip}(i, k) &= F_2(n_{ep}(i, k), T(i, k)) \end{aligned} \quad (74)$$

and

$$\sigma_{ep}(i, k) = \frac{\sigma_{enp}(i, k)\sigma_{eip}(i, k)}{\sigma_{enp}(i, k) + \sigma_{eip}(i, k)}. \quad (75)$$

For the  $n^{th}$  time step advance from time  $t^n$  to time  $t^n + \Delta t = t^{n+1}$  we begin with the number densities  $n_e^n(i, k), n_+^n(i, k), n_-^n(i, k), n_o^n(i, k)$  for the ionization electrons, positive ions, negative ions, and neutral molecules. We also have the electric field  $er^n(i, k), ez^n(i, k)$ . We will initialize the final electric field  $er^{n+1}(i, k), ez^{n+1}(i, k)$  to  $er^n(i, k), ez^n(i, k)$  and then iterate until the change in  $er^{n+1}(i, k), ez^{n+1}(i, k)$  is acceptable. Therefore we start the iteration by setting

$$\begin{aligned} er^{n+1}(i, k) &= er^n(i, k) \\ ez^{n+1}(i, k) &= ez^n(i, k) \\ er\_temp(i, k) &= er^n(i, k) \\ ez\_temp(i, k) &= ez^n(i, k). \end{aligned} \quad (76)$$

We now loop over the  $j$  index. The first step is to define time averaged fields

$$\begin{aligned} e\tilde{r}(i, k) &= 0.5(er^n(i, k) + er^{n+1}(i, k)) \\ e\tilde{z}(i, k) &= 0.5(ez^n(i, k) + ez^{n+1}(i, k)). \end{aligned} \quad (77)$$

These fields are not located at the fluid cell center but rather at the edges. Therefore we take spatial averages

$$\begin{aligned}
\langle e\tilde{r}(i,k) \rangle &= 0.5(e\tilde{r}(i,k) + e\tilde{r}(i-1,k)) \\
\langle e\tilde{z}(i,k) \rangle &= 0.5(e\tilde{z}(i,k) + e\tilde{z}(i,k-1)) \\
emag(i,k) &= \left| \langle e\tilde{r}(i,k) \rangle^2 + \langle e\tilde{z}(i,k) \rangle^2 \right|
\end{aligned} \tag{78}$$

at the fluid cell centers ( $x(i), z(k)$ ) and calculate the mobilities, rate coefficients, and drift velocities as was done for the one dimensional case and drift velocities as was done for the one dimensional case. For air we have

$$\mu_e(i,k) \cong \frac{1}{\rho_r} \left\{ \begin{array}{ll} 0.79 & , emag(i,k) / \rho_r < 3 \times 10^3 V / m \\ 0.25 \sqrt{3 \times 10^4 \rho_r / emag(i,k)} & , 3 \times 10^3 < emag(i,k) / \rho_r < 3 \times 10^5 V / m \\ 0.079 & , emag(i,k) / \rho_r > 3 \times 10^5 V / m \end{array} \right\} \tag{79}$$

$$\mu_p(i,k) = 2.4 \times 10^{-4} / \rho_r \tag{80}$$

$$\alpha(i,k) = 4.33 \times 10^5 \rho_r \exp \left( \frac{-1.98 \times 10^7}{emag(i,k) / \rho_r} \right) \tag{81}$$

$$A(i,k) \cong 10^8 \rho_r^2 \tag{82}$$

$$R_{ei}(i,k) = 2 \times 10^{-13} \tag{83}$$

$$R_{ii}(i,k) = 2 \times 10^{-12} \rho_r \tag{84}$$

$$\begin{aligned}
v_{r_e}(i,k) &= -\mu_e(emag(i,k)) \cdot \langle e\tilde{r}(i,k) \rangle \\
v_{z_e}(i,k) &= -\mu_e(emag(i,k)) \cdot \langle e\tilde{z}(i,k) \rangle \\
v_{r_+}(i,k) &= \mu_p(emag(i,k)) \cdot \langle e\tilde{r},k \rangle \\
v_{z_+}(i,k) &= \mu_p(emag(i,k)) \cdot \langle e\tilde{z},k \rangle \\
v_{r_-}(i,k) &= -\mu_p(emag(i,k)) \cdot \langle e\tilde{r}(i,k) \rangle \\
v_{z_-}(i,k) &= -\mu_p(emag(i,k)) \cdot \langle e\tilde{z}(i,k) \rangle
\end{aligned} \tag{85}$$

$$\begin{aligned}
C(i,k) &= \alpha(i,k) |v_e(i,k)| \\
B(i,k) &= \delta^i |v_e(i,k)| \\
E(i,k) &= 1 / \tau_m.
\end{aligned} \tag{86}$$

We also need to calculate the mobilities and drift velocities at the fluid cell edges (the  $xo(i)$  and  $zo(k)$  locations in Figure 2) i.e. we replace  $emag(i, k) = \sqrt{\langle e\tilde{r}(i, k) \rangle^2 + \langle e\tilde{z}(i, k) \rangle^2}$  with  $emag(i, k) = \sqrt{e\tilde{r}(i, k)^2 + e\tilde{z}(i, k)^2}$  and recalculate the mobilities given above. We then define the drift velocities

$$\begin{aligned}
\langle v_{r_e}(i) \rangle &= -\mu_e(emag(i)) \cdot e\tilde{r}(i) \\
\langle v_{z_e}(i) \rangle &= -\mu_e(emag(i)) \cdot e\tilde{z}(i) \\
\langle v_{r_+}(i) \rangle &= \mu_p(emag(i)) \cdot e\tilde{r}(i) \\
\langle v_{z_+}(i) \rangle &= \mu_p(emag(i)) \cdot e\tilde{z}(i) \\
\langle v_{r_-}(i) \rangle &= -\mu_p(emag(i)) \cdot e\tilde{r}(i) \\
\langle v_{z_-}(i) \rangle &= -\mu_p(emag(i)) \cdot e\tilde{z}(i).
\end{aligned} \tag{87}$$

For nitrogen we have (MKS units)

$$\mu_e(i, k) = \frac{1}{\rho_r} \begin{cases} 3.8 \times 10^{-2} & , emag(i, k) / \rho_r < 1.14 \times 10^7 \text{ V / m} \\ 3.8 \times 10^{-2} \sqrt{1.14 \times 10^7 \rho_r / emag(i, k)} & , emag(i, k) / \rho_r \geq 1.14 \times 10^7 \text{ V / m} \end{cases} \tag{88}$$

$$\mu_p(i, k) = 3.4 \times 10^{-4} / \rho_r \tag{89}$$

$$\alpha(i, k) = 4.33 \times 10^5 \rho_r \exp\left(\frac{-1.98 \times 10^7}{emag(i, k) / \rho_r}\right) \tag{90}$$

$$A(i, k) = 0 \tag{91}$$

$$R_{ei}(i, k) = 2 \times 10^{-13} \tag{92}$$

$$R_{ii}(i, k) = 2 \times 10^{-12} \rho_r. \tag{93}$$

As in the one dimensional case we need to determine the UV electron sources and the UV induced photoemission at the cathode. For the UV electron sources we will assume that only electron collisions on the axis are important. As a result we can write

$$S_e(i, k) = A \sum_{k'=1}^{k \max} \langle \dot{n}_D(1, k') \rangle S_{\text{int}}(i, k, k') \tag{94}$$

where  $S_e(i, k)$  has units of electrons per unit volume per unit time and



$$\begin{aligned}
S_{\text{int}}(i, k, k') &= \frac{\psi(R'P) \cdot P \cdot \Delta V(1, k')}{4\pi R'^2} \\
R'^2 &= r(i)^2 + (z(k) - zo(ki))^2 \\
\Delta V(1, k') &= \pi r o(1)^2 \Delta z(k') \\
\langle \dot{n}_D(1, k) \rangle &= 0.5 (C(1, k) n_e(1, k) + C(1, k+1) n_e(1, k+1)).
\end{aligned} \tag{95}$$

The  $A$  coefficient is an empirical scale factor to account for the fact that the discharge has a radius larger than one cell. It would be expected that  $A \sim$  the number of radial cells in the discharge.

For the UV induced photoemission we first determine an electron emission flux at the cathode defined by

$$\Gamma_e^+(i_c, k_c) = Y_p(e/p) B \sum_{k'=1}^{k_{\max}} (\hat{e}_n \cdot \hat{\Omega}) \langle S_p(1, k') \rangle Y_{\text{int}}(i_c, k_c, 1, k') \tag{96}$$

where  $S_p(1, k')$  has units of photons per unit volume per unit time and

$$\begin{aligned}
Y_{\text{int}}(i_c, k_c, 1, k') &= \frac{e^{-\mu(R'P)R'P} \Delta V(1, k')}{4\pi R'^2} \\
(\hat{e}_n \cdot \hat{\Omega}) &= \begin{cases} \frac{zo(k') - z(k_c)}{R(i_c)}, & i_c > 1 \\ 1, & i_c > 1 \end{cases} \\
R'^2 &= r(i_c)^2 + (z(k_c) - zo(k'))^2 \\
\Delta V(1, k') &= \pi r o(1)^2 \Delta z(k') \\
S_p(1, k') &= \left( \frac{n_m^*(1, k')}{\tau_m^i(1, k')} \right).
\end{aligned} \tag{97}$$

The first term in the sum represents the  $\hat{e}_n \cdot \hat{\Omega}$  cosine term in the integration over the emitting surface. The units of the absorption coefficient are  $length^{-1} pressure^{-1}$ . As a result the integral  $Y_{\text{int}}(i_c, i')$  has units of length. Given the electron emission flux the electron source at the cathode is given by

$$S_e(i_c, k_c) = \frac{\Gamma_e^+(i_c, k_c)}{zo(k_c) - zo(k_c - 1)}. \text{ th} \tag{98}$$

As in the one dimensional case after the air chemistry and UV sources are called the electron and ion transport terms are determined using a second order upwind differencing scheme. We define the advective fluxes as

$$\begin{aligned}\Gamma_{x_{adv}}(i,k) &= \begin{cases} n(i,k)\langle \nu r(i,k) \rangle, \langle \nu r(i,k) \rangle \geq 0 \\ n(i+1,k)\langle \nu r(i,k) \rangle, \langle \nu r(i,k) \rangle < 0 \end{cases} \\ \Gamma_{z_{adv}}(i,k) &= \begin{cases} n(i,k)\langle \nu z(i,k) \rangle, \langle \nu z(i,k) \rangle \geq 0 \\ n(i+1,k)\langle \nu r(i,k) \rangle, \langle \nu r(i,k) \rangle < 0 \end{cases}.\end{aligned}\quad (99)$$

We also include the diffusion terms

$$\begin{aligned}\Gamma_{r_{diff}}(i,k) &= -\frac{D}{\Delta r(i)}(n^n(i+1,k) - n^n(i,k)) \\ \Gamma_{z_{diff}}(i,k) &= -\frac{D}{\Delta z(k)}(n^n(i,k+1) - n^n(i,k)).\end{aligned}\quad (100)$$

The transport terms are now advanced using

$$\begin{aligned}[\bar{\nabla} \cdot (n\bar{v})] + [\bar{\nabla} \cdot \bar{\Gamma}_{diff}] &= \frac{1}{\Delta V(i,k)} \left\{ \Gamma_{r_{adv}}(i,k)AR(i,k) - \Gamma_{r_{adv}}(i-1,k)AR(i-1,k), \quad \nu r(i,k) \geq 0 \right\} \\ &\quad + \frac{1}{\Delta V(i,k)} \left\{ \Gamma_{r_{adv}}(i+1,k)AR(i,k) - \Gamma_{r_{adv}}(i,k)AR(i-1,k), \quad \nu r(i,k) < 0 \right\} \\ &\quad + \frac{1}{\Delta V(i,k)} \left\{ \Gamma_{z_{adv}}(i,k)AZ(i,k) - \Gamma_{z_{adv}}(i,k-1)AZ(i,k-1), \quad \nu z(i,k) \geq 0 \right\} \\ &\quad + \frac{1}{\Delta V(i,k)} \left\{ \Gamma_{z_{adv}}(i,k+1)AR(i,k) - \Gamma_{z_{adv}}(i,k)AR(i,k-1), \quad \nu z(i,k) < 0 \right\} \\ &\quad + \frac{1}{\Delta V(i,k)} (\Gamma_{x_{diff}}(i,k)AR(i,k) - \Gamma_{x_{diff}}(i-1,k)AR(i-1,k)) \\ &\quad + \frac{1}{\Delta V(i,k)} (\Gamma_{z_{diff}}(i,k)AZ(i,k) - \Gamma_{z_{diff}}(i,k-1)AZ(i,k-1)).\end{aligned}\quad (101)$$

Given the advective flux the current density is given by

$$\begin{aligned}cur(i,k) &= e\Gamma_{r_{adv}}(i,k) \\ cuz(i,k) &= e\Gamma_{z_{adv}}(i,k).\end{aligned}\quad (102)$$

the change in number densities due to advection and diffusion must be combined with the growth or decay terms due to avalanche, attachment, recombination, and so on. Once the number densities are advanced the early time electrical conductive is calculated from

$$\sigma(i,k) = |e| \left( \mu_e(i,k)n_e^{n+1}(i,k) + \mu_p(i,k)(n_+^{n+1}(i,k) + n_-^{n+1}(i,k)) \right). \quad (103)$$

This conductivity is not directly used in the calculation but serves as a diagnostic. Next the electrode and wall boundary conditions are set using the modmap (i,k) array. The net charge density is determined from

$$\rho^{n+1}(i,k) = e(n_e^{n+1}(i,k) - n_+^{n+1}(i,k) + n_-^{n+1}(i,k)) \quad (104)$$

and the total net charge is

$$Q_{total}^{n+1} = \sum_{k=1}^{nez} \sum_{i=1}^{ner} \rho^{n+1}(i, k) \Delta V(i, k). \quad (105)$$

In order to account for the resistance of the power supply it is necessary to calculate an effective discharge current between the electrodes, assumed to be located at grid points  $id\_lower$  and  $id\_upper$  respectively. We have

$$I_d = \frac{\sum_{kd\_lower}^{kd\_upper-1} \sum_{i=1}^{ner} cu_z(i, k) AZ(i, k) \Delta z(k)}{\sum_{kd\_lower}^{kd\_upper-1} \Delta z(k)}. \quad (106)$$

Now we will adjust the potential at the electrons using the source resistance  $R_s$  of the power supply i.e.

$$\phi(id\_upper) - \phi(id\_lower) = (V_{id\_upper} - V_{id\_lower}) - R_s I_d. \quad (107)$$

The Poisson equation solver described previously is called to solve

$$\nabla^2 \phi^{n+1} = \frac{e}{\epsilon_o} (n_e^{n+1} - n_+^{n+1} + n_-^{n+1}) \quad (108)$$

and the fields are advanced as

$$\bar{e}^{n+1} = -\bar{\nabla} \phi^{n+1}. \quad (109)$$

We now check the convergence of the iteration by checking

$$\max \left| \frac{\bar{e}^{n+1}(i, k) - \bar{e}_{temp}(i)}{\bar{e}^{n+1}(i) + 1.0 \times 10^{-12}} \right| < 0.001 \quad (110)$$

or noting that the number of iterations  $j \geq j_{\max}$ . If the exit criteria are not met we set

$$\begin{aligned} er\_temp(i, k) &= er^{n+1}(i, k) \\ ez\_temp(i, k) &= ez^{n+1}(i, k) \end{aligned} \quad (111)$$

and repeat. If the exit criteria are met we proceed and determine the number of electrons and positive ions per unit area i.e.

$$\begin{aligned}
N_e^{n+1} &= \sum_1^{nez} \sum_1^{ner} n_e^{n+1}(i, k) \Delta V(i, k) \\
N_+^{n+1} &= \sum_1^{nez} \sum_1^{ner} n_+^{n+1}(i, k) \Delta V(i, k).
\end{aligned} \tag{112}$$

This completes the early time advance where propagations effects are important and where the electron temperature is not in equilibrium with the neutral molecules. However, we need to advance Plooster's equations for the neutral gas specific energy, temperature, and conductivity in order to know when to switch over to the late time model. The specific energy is advanced by considering the thermal energy density with contributions to both the early time electron flow and the heating from the Plooster conductivity. Specifically we advance

$$\begin{aligned}
\langle J \cdot E \rangle &= 0.5 \left( (er(i-1, k)cur(i-1, k) + er(i, k)cur(i, k)) + (ez(i, k-1)cuz(i, k-1) + ez(i, k)cuz(i, k)) \right) \\
\langle ER\_ave \rangle &= 0.5 (er(i-1, k) + er(i, k)) \\
\langle EZ\_ave \rangle &= 0.5 (ez(i, k-1) + ez(i, k)) \\
(\rho \varepsilon) &= \rho_o \varepsilon^n(i, k) + \langle J \cdot E \rangle \Delta t + \sigma_{ep}(i, k) \left( \langle ER\_ave \rangle^2 + \langle EZ\_ave \rangle^2 \right) \Delta t \\
\varepsilon^{n+1}(i, k) &= (\rho \varepsilon) / \rho_o.
\end{aligned} \tag{113}$$

In order to determine the temperature we need to invert Plooster's equation of state. The method for determining temperature goes as follows. Given the specific internal energy density  $\varepsilon^{n+1}$  the temperature  $T^{n+1}$  can be determined by forming the function

$$g(T^{n+1}) = \varepsilon(T^{n+1}, \rho) - \varepsilon^{n+1} = 0. \tag{114}$$

Then by Newton-Raphson iteration

$$\begin{aligned}
T^{n+1}(j+1) &= T^{n+1}(j) - \frac{g(T^{n+1}(j))}{\partial g(T^{n+1}(j)) / \partial T} \\
&= T^{n+1}(j) - \frac{(\varepsilon(T^{n+1}(j), \rho) - \varepsilon^{n+1}) \Delta T}{\varepsilon(T^{n+1}(j) + \Delta T, \rho) - \varepsilon(T^{n+1}(j), \rho)}.
\end{aligned} \tag{115}$$

The  $\Delta T$  term can be set to about  $T^n \cdot 10^{-3}$ .

The Plooster conductivity  $\sigma_{ep}(i, k)$  is advanced as described previously. The resistance array between the fluid cell, shown in Figure 7, centers is determined as follows. For the vertical resistors on the axis we have ( $i = 1, k = 1, nhz$ )

$$RZ(1, k) = \frac{zo(k) - z(k)}{\pi ro(1)^2 \sigma_{ep}(1, k)} + \frac{z(k+1) - zo(k)}{\pi ro(1)^2 \sigma_{ep}(1, k+1)}. \tag{116}$$

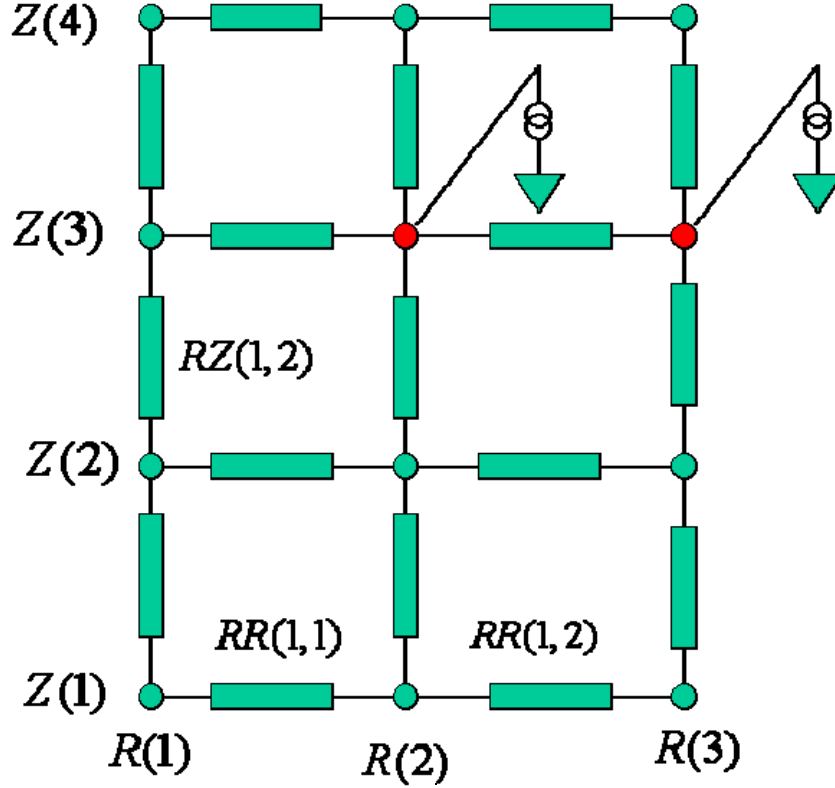


Figure 7. Representation of the finite difference conductivity/resistivity mesh used to solve for the late time discharge. Note that objects with fixed potentials are represented by current sources.

For the inner vertical resistors ( $i = 2, \dots, nhr, k = 1, nhz$ ) we have

$$RZ(i, k) = \frac{zo(k) - z(k)}{\pi(ro(i)^2 - ro(i-1)^2)\sigma_{ep}(i, k)} + \frac{z(k+1) - zo(k)}{\pi(ro(i)^2 - ro(i-1)^2)\sigma_{ep}(i, k+1)}. \quad (117)$$

For the outer vertical resistors ( $i = ner, k = 1, nhz$ ) we have

$$RZ(ner, k) = \frac{zo(k) - z(k)}{\pi(r(ner)^2 - ro(nhr)^2)\sigma_{ep}(ner, k)} + \frac{z(k+1) - zo(k)}{\pi(r(ner)^2 - ro(nhr)^2)\sigma_{ep}(ner, k+1)}. \quad (118)$$

Normally the outer boundary is conductive so these resistors are set to a small value. For the interior radial resistors ( $i = 1, \dots, nhr, k = 2, \dots, nhz$ ) we have

$$\begin{aligned}
RR(i,1) &= \frac{ro(i) - r(i)}{2\pi ro(i)\Delta z(1)\sigma_{ep}(i,1)} + \frac{r(i+1) - ro(i)}{2\pi ro(i)\Delta z(1)\sigma_{ep}(i+1,1)} \\
RR(i,k) &= \frac{ro(i) - r(i)}{2\pi ro(i)(zo(k) - zo(k-1))\sigma_{ep}(i,k)} + \frac{r(i+1) - ro(i)}{2\pi ro(i)(zo(k) - zo(k-1))\sigma_{ep}(i+1,k)} \\
RR(i,nez) &= \frac{ro(i) - r(i)}{2\pi ro(i)\Delta z(nhz)\sigma_{ep}(i,nez)} + \frac{r(i+1) - ro(i)}{2\pi ro(i)\Delta z(nhz)\sigma_{ep}(i+1,nez)}.
\end{aligned} \tag{119}$$

The radial resistors across the bottom and top of the mesh form the conductive boundary condition so they are also set to a small value as are the resistances inside any conductive object within the finite difference mesh.

At this point we need to calculate the voltages at the cell nodes and the electric fields. There are two approaches to consider. The first is to approximate the resistance between two objects or potential surfaces within the finite difference mesh by assuming axial current flow. In this case we can divide the problem into a set of conductive disks in series. The admittance of each disk is given by

$$Y(k) = \sum_{i=1}^{i_{upper}} 1.0 / RZ(i, k) \tag{120}$$

and the Plooster resistance between the two electrodes is given by

$$R_{plooster} = \sum_{k=kd_{lower}}^{kd_{upper}} 1.0 / Y(k). \tag{121}$$

## 4.0 Test Simulations

In order to test the Poisson solver, a couple of simple problems have been solved. In both cases, the program was applied to a problem with 128  $r$  grid cells and 256  $z$  grid cells. Both the  $r$  and the  $z$  are uniform, with a cell size of one half unit. The first test case is for a sphere of uniform charge density of magnitude 1/10. The sphere has a radius of five units. Figure 8 shows the charge density used. The potential computed from this charge distribution is shown in Figure 9.

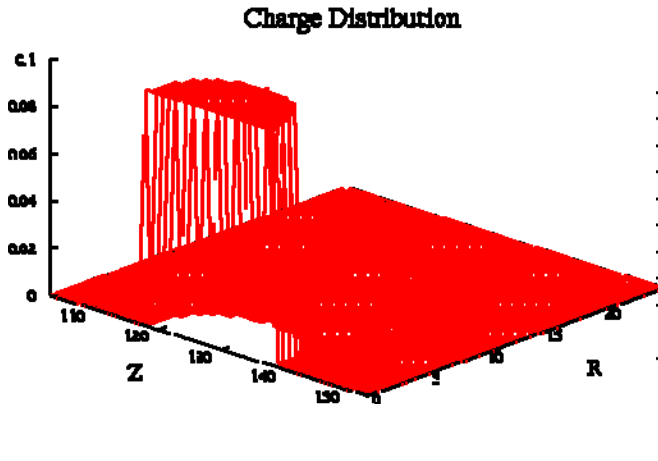


Figure 8: Test Run Charge Density.

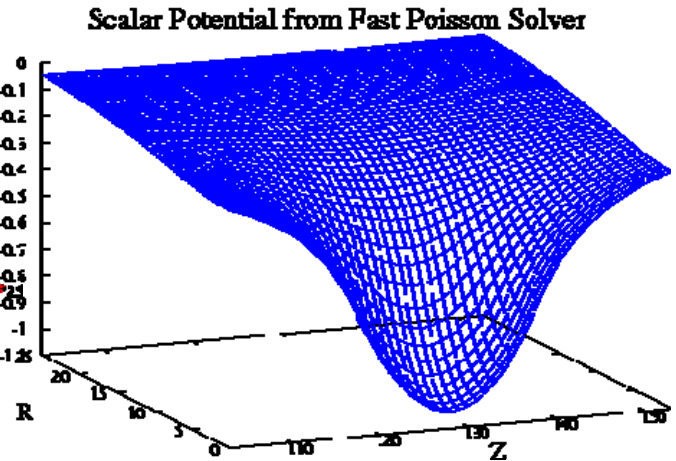


Figure 9: Test Run Scalar Potential.

This is a particularly nice test case because the solution of the resulting equation is known analytically. In particular, consider solving Poisson's equation solved for a uniformly charged sphere at the origin

$$\nabla^2 \phi = \begin{cases} \rho_0 & 0 \leq r \leq a \\ 0 & a < r. \end{cases} \quad (122)$$

In spherical-polar coordinates, symmetry requires  $\frac{\partial \phi}{\partial \theta} = \frac{\partial \phi}{\partial \varphi} = 0$ , and we are left with an equation in the radial variable only:

$$\frac{1}{r^2} \frac{\partial}{\partial r} \left\{ r^2 \frac{\partial \phi}{\partial r} \right\} = \begin{cases} \rho_0 & 0 \leq r \leq a \\ 0 & a < r. \end{cases} \quad (123)$$

Multiplying by  $r^2$  and integrating with respect to  $r$  once gives

$$r^2 \frac{\partial \phi}{\partial r} = \begin{cases} \frac{\rho_0}{3} r^3 + c_1 & 0 \leq r \leq a \\ c_2 & a < r. \end{cases} \quad (124)$$

Dividing by  $r^2$  and integrating with respect to  $r$  again gives

$$\phi = \begin{cases} \frac{\rho_0}{6} r^2 - \frac{c_1}{r} + c_3 & 0 \leq r \leq a \\ -\frac{c_2}{r} + c_4 & a < r. \end{cases} \quad (125)$$

The first constant of integration may be determined by a regularity condition. The potential must be finite as  $r \rightarrow 0$  which forces  $c_1$  to be zero. We also require that the potential must go to zero as  $r$  becomes infinite. This forces  $c_4$  to be zero. A requirement that the potential and its first (radial) derivative are continuous everywhere, but at  $r = a$  in particular, gives two equations that may be solved for  $c_2$  and  $c_3$ .

$$\frac{1}{6} \rho_0 a^2 + c_3 = -\frac{c_2}{a} \quad (126)$$

and

$$\frac{1}{3} \rho_0 a = \frac{c_2}{a^2} \quad (127)$$

result in

$$c_2 = \frac{1}{3} \rho_0 a^3; c_3 = -\frac{1}{2} \rho_0 a^2 \quad (128)$$

finally giving the solution

$$\phi = \begin{cases} \frac{\rho_0}{6} r^2 - \frac{1}{2} \rho_0 a^2 & 0 \leq r \leq a \\ -\frac{1}{3} \frac{\rho_0 a^3}{r} & a < r. \end{cases} \quad (129)$$

The scalar potential given by this analytical solution for a sphere analogous to the one used in Figure 9 is shown in Figure 10. The difference between the analytic solution and the one obtained from the fast Poisson solver is shown in Figure 11.



There are two primary causes for the difference in the values of the analytic potential and the computed one. The first is that, due to discretization, the charged objects are slightly different. This is clearly seen in Figure 11 where the error has large peaks near the boundary of the charged sphere. The second source of error is due to the fact that, for the numerical solution, the scalar potential is forced to be zero at a cylinder defined by (polar) radius  $r = R$  and with the top and bottom defined by  $z = 0$  and  $z = Z$ , respectively. The analytic solution asymptotically approaches zero as the (spherical) radius becomes large, but is not zero for any finite value.

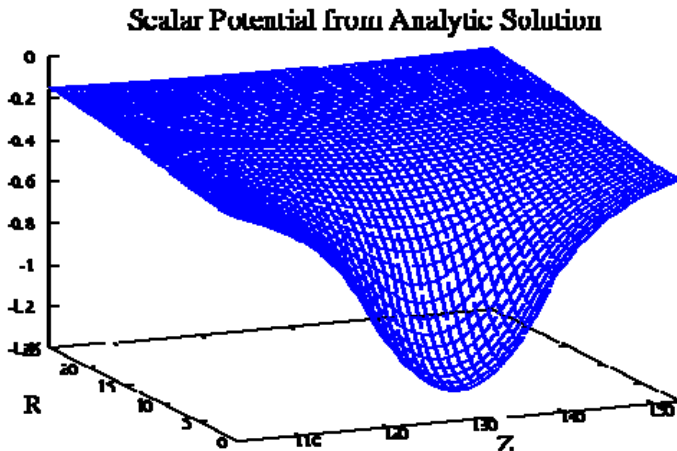


Figure 10: Analytic Scalar Potential for a Uniformly Charge Sphere.

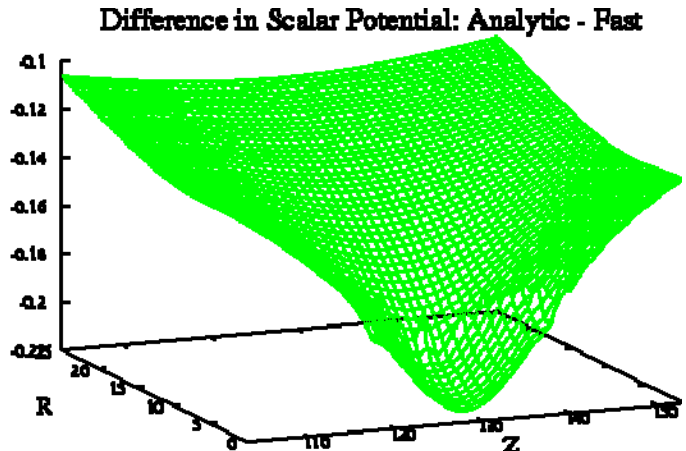


Figure 11: Difference between Analytic and Fast Poisson Solutions.

To give the algorithm a bit more of a challenge, a second test case was run. In this case, two spheres of equal but opposite charges are displaced from the center of the grid by three units, each in a different direction. This results in two equal, but opposite crescent shaped charge objects. In the area near the origin where the two spheres overlap results in a cancellation of charge. Figure 12 shows the resulting charge density for this run. Figure 13 shows the resulting scalar potential computed from the charge distribution of Figure 12.

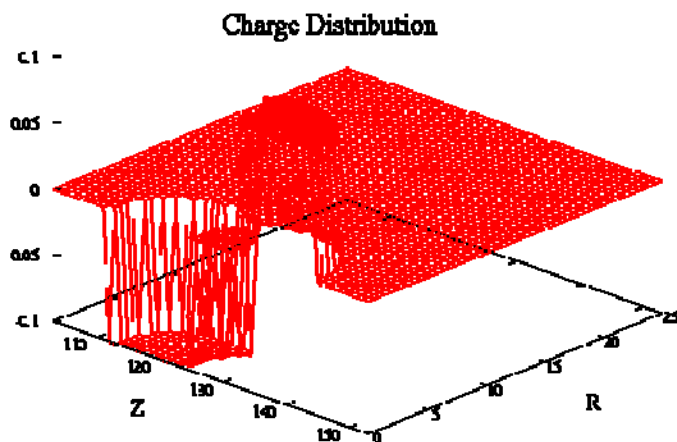


Figure 12: Charge Distribution for Second Test Case.

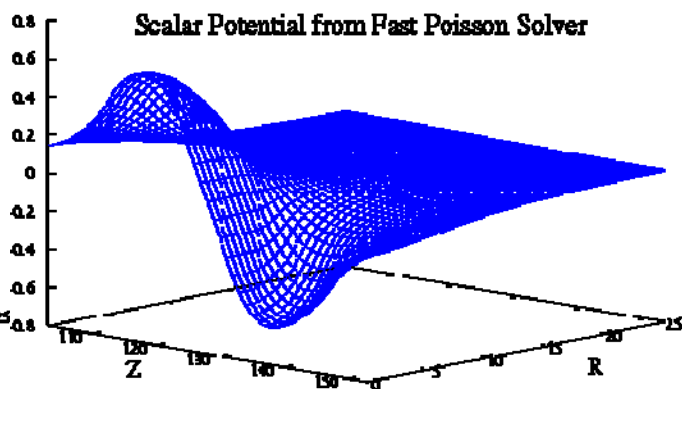


Figure 13: Scalar Potential for Second Test Case.

## 5.0 Conclusions

Numerical models have been developed for the range of physical process on spatial and temporal scales required for the analysis of the USP Laser initiated high voltage discharge problem. These specifically include:

- Treatment of the reaction rate equations for determining the evolution of the numerous charged particle species in air under high electric field strengths. This treatment is used in the early time discharge initiation phase of the process.
- A very fast method for determining the quasi-static values of the electric field throughout the simulation volume, at each time step of the simulation. This was accomplished by development of an FFT/Cubic Spline based Poisson algorithm.
- A simulation of the production and absorption of ionizing uv radiation within the computational volume.
- A method for representing various metallic object boundary conditions within the overall cylindrically symmetric simulation volume and still allow for the zero field end boundaries required by the FFT based Poisson algorithm. This method employs the placement of a fictitious charge distribution that yields the proper boundary conditions for imbedded conducting surfaces.
- A simulation of the motion of electrons within the simulation volume, this was treated with a two step fluid description of the moving electrons.

In order to extend the computational range within feasible computer simulation time approximations were developed for use in the early and late time phases of the simulation:

- An approximation was developed, for use in late time after charge flow equilibration, to treat the electron motion as a current with a conductivity based on an equation of state previously developed by Plooster.
- Definition of a procedure to treat long range (Meter scale) discharges as a series of detailed local ‘snap shot’ calculations at points along the extended streamer path.

The above outlined models were integrated and demonstrated on a single CPU PC based workstation. Test simulations were done to assure the proper operation of the simulation modules. Methods for parallelizing the overall simulation for porting to a multi-core High Performance Computer were studied and outlined.

The modules outlined above were however integrated and a series of small scale test problems completed. These calculations showed the apparent proper behavior of the simulation, the expected reduction of the air breakdown voltage associated with the discharge, and the formation and initial propagation of a discharge channel were observed. Larger scale calculations were not feasible on a workstation type computer. Methods for moving to parallel operation on an HPC were investigated and outlined.

## 6.0 References

- 1 - W. Zimmerman, B. Fisk, V. Van Lint, N. Carron, W. Page "Ultra-Short Pulse Laser Analysis Studies" AFRL-DE-PS-TR-2005-1063, August, 2005
- 2 - Braun, G. Korn, X. Liu, D. Du, J. Squier, and G. Mourou, "Self-Channeling of high-peak-power femtosecond laser pulses in air," *Optics Letters*, Vol. 20, No. 1 January 1, 1995, pg 73
- 3 - M. Mlejnek, E. M. Wright, J. V. Moloney, "Dynamic spatial replenishment of femtosecond pulses propagation in air," *Optics Letters*, Vol. 23, No. 5 March 1998, pg 382.
- 4 - P. Sprangle, J. R. Penano, and B. Hafizi, "Propagation of intense short laser pulses in the atmosphere," *Physical Review* 3, Vol. 66, 2002, pg 046418-1
- 5 - L. E. Kline and J. G. Siambis, "Computer Simulation of Electrical Breakdown in Gases; Avalanche and Streamer Formation," *Physical Review A*, Volume 5, Number 2, February 1972.
- 6 - G. W. Penny and G. T. Hummert, "Photoionization Measurements in Air, Oxygen, and Nitrogen," *Journal of Applied Physics*, Volume 41, Number 2, February 1970.
- 7 - E. E. Kunhardt and Y. Tzeng, (1)"Monte Carlo Technique for Simulating the Evolution of an Assembly of Particles Increasing in Number," *Journal of Computational Physics*, Volume 67, 1986, page 279.
- 8 - K. Yoshida and H. Tagashira, "Computer simulation of a nitrogen discharge considering the radial electron drift," *Journal Physics D: Applied Physics*, Volume 9, 1976, page 485.
- 9 - C. Wu and E. E. Kunhardt, "Formation and propagation of streamers in N<sub>2</sub> and N<sub>2</sub>-SF<sub>6</sub> mixtures," *Physical Review A*, Volume 37, Number 11, June 1, 1988, page 4396.
- 10 - M. C. Wang and E. E. Kunhardt, "Streamer dynamics," *Physical Review A*, Volume 42, Number 4, August 15, 1990, page 2366.
- 11 - P. A. Vitello, B. M. Penetrante, and J. N. Bardsley, "Simulation of negative-streamer dynamics in nitrogen," *Physical Review E*, Volume 49, Number 6, June 1994, page 5574.
- 12 - A. Kulikovsky, "The structure of streamers in N<sub>2</sub>, I: fast method of space charge dominated plasma simulation, *Journal Physics D: Applied Physics*, Volume 27, 1994, page 2556
- 13 - In-Ming Guo and Chwan-Hwa "John" Wu, "Comparisons of multidimensional non-equilibrium and equilibrium fluid and Monte Carlo models for streamers," *Journal Physics D: Applied Physics*, Volume 26, 1993, page 487.
- 14 - Plooster, "Numerical Simulation of Spark Discharges in Air," *The Physics of Fluids*, Volume 14, Number 10, October, 1971, page 2111.

- 15 - Ganesh, A. Rajabooshanam, and S. K. Dhali, "Numerical studies of streamer to arc transition," *Journal Applied Physics*, Volume 72, Number 9, November 1, 1992, page 3957.
- 16 - A. Kossyi, A. Yu Kostinsky, A. A. Matveyev and V. P. Silakov, "Kinetic scheme of the non-equilibrium discharge in nitrogen-oxygen mixtures," *Plasma Sources Science Technology*, Volume 1, 1992, page 207.
- 17 - V. Naidis, "On streamer interaction in a pulsed positive corona discharge," *Journal Physics D: Applied Physics*, Volume 29, 1996, page 779.
- 18 - L. Aleksandrov and E. M. Bazelyan, "Temperature and density effects on the properties of a long positive streamer in air," *Journal Physics D: Applied Physics*, Volume 29, 1996, page 2873.
- 19 - Aleksandrov, E. M. Bazelyan and A. M. Konchakov, (1) "Plasma Parameters in the Channel of a Long Leader in Air," *Plasma Physics Reports*, Volume 27, Number 10, 2001, page 875.
- 20 - L. Aleksandrov and E. M. Bazelyan, (2) "Streamer Breakdown of Long Gas Gaps," *Plasma Physics Reports*, Volume 27, Number 12, 2001, page 1057.
- 21 - L. Aleksandrov, E. M. Bazelyan and A. M. Konchakov, "Evolution of the Channel of a Long Leader in Air after a Sharp Decrease in the Discharge Current," *Plasma Physics Reports*, Volume 29, Number 3, 2003, page 220.
- 22 - M. Bazelyan and Yu. P. Raizer, *Spark Discharge*, CRC Press, 1998
- 23 - Capitelli, C. M. Ferreira, B. F. Gordiets and A. I. Osipov, *Plasma Kinetics in Atmospheric Gases*, Springer, 2000.
- 24 - R. L. Gardner, M. H. Frese, J. L. Gilbert and C. L. Longmire, "A Physical Model of Nuclear Lightning," *Phys. Fluids*, Vol. 27, No. 11, November, 1984.
- 25 - .Kunhardt and P. F. Williams. "Direct Solution of Poisson's Equation in Cylindrically Symmetric Geometry: A Fast Algorithm," *Journal of Computational Physics*, Vol. 57. 1985, page 403
- 26 - Hockney, "The Potential Calculation and Some Applications," Methods in Computational Physics, Vol. 9. Academic Press, New York, 1970, page 135.
- 27 - M. Plooster, "Shock Waves from Line Sources. Numerical solutions and Experimental Measurements," *The Physics of Fluids*, Vol. 13, No 11, November, 1970, page 2665.
- 28 - M.J. Quinn, Parallel Programing in C with MPI and OpenMP, McGraw Hill, New York, 2004, page 353.
- 29 - The LAM/MPI Team, The LAM/MPI User's Guide, Version 7.2.1, Pervasive Technology Labs at the University of Indiana, 2006. [www.lam-mpi.org](http://www.lam-mpi.org)

30 - C. L. Longmire and J. L. Gilbert, "Theory of EMP Coupling in the Source Region," Defense Nuclear Agency, DNA5687F, February, 1980.

31 - C. L. Longmire, "On the Electromagnetic Pulse Produced by Nuclear Explosions," IEEE Transactions on Antennas and Propagation, Volume AP-26, Number 1, January, 1978, page 3.

32 - L. Brode, "Review of Nuclear Weapons Effects," Annual Review of Nuclear Science, E. Segre, J. R. Grover, and H. P. Noyes, Volume 18, 1968, page 153.

33 - H. Press, B. P. Flannery, S.A. Teukolsky and W. T. Vetterling, Numerical Recipes, Cambridge University Press, 1986.

## Distribution List

DTIC/OCF 8725 John J. Kingman Rd. Suite 094 Ft Belvoir, VA 22060-6218	1 cy
AFRL/RVIL Kirtland AFB, NM 87117-5776	2 cys
Official Record Copy AFRL/RDLS/William Page	2 cys